

MULTI-WAVELENGTH STUDIES OF SPECTACULAR RAM-PRESSURE STRIPPING OF A GALAXY. II. STAR FORMATION IN THE TAIL

MASAFUMI YAGI¹, LIYI GU^{2,3}, YUTAKA FUJITA⁴, KAZUHIRO NAKAZAWA², TAKUYA AKAHORI⁵,
 TAKASHI HATTORI⁶, MICHITOSHI YOSHIDA⁷, AND KAZUO MAKISHIMA^{2,3,8}

¹ Optical and Infrared Astronomy Division, National Astronomical Observatory of Japan,
 2-21-1 Osawa, Mitaka, Tokyo 181-8588, Japan; YAGI.Masafumi@nao.ac.jp

² Department of Physics, The University of Tokyo, 7-3-1 Hongo, Bunkyo-ku, Tokyo 113-0011, Japan

³ Research Center for Early Universe, School of Science, The University of Tokyo, 7-3-1 Hongo, Bunkyo-ku, Tokyo 113-0011, Japan

⁴ Department of Earth and Space Science, Graduate School of Science, Osaka University, Toyonaka, Osaka 560-0043, Japan

⁵ Sydney Institute for Astronomy, School of Physics, The University of Sydney, 44 Rosehill Street, Redfern, NSW 2006, Australia

⁶ Subaru Telescope, 650 North A'ohoku Place, Hilo, HI 96720, USA

⁷ Hiroshima Astrophysical Science Center, Hiroshima University, 1-3-1 Kagamiyama, Higashi-Hiroshima, Hiroshima 739-8526, Japan

⁸ MAXI Team, Institute of Physical and Chemical Research, 2-1 Hirosawa, Wako, Saitama 351-0198, Japan

Received 2013 August 27; accepted 2013 September 20; published 2013 November 7

ABSTRACT

With multiband photometric data in public archives, we detected four intracluster star-forming regions in the Virgo Cluster. Two of them were at a projected distance of 35 kpc from NGC 4388 and the other two were 66 kpc away. Our new spectroscopic observations revealed that their recessional velocities were comparable to the ram-pressure-stripped tail of NGC 4388 and confirmed the association. The stellar mass of the star-forming regions ranged from 10^4 to $10^{4.5} M_{\odot}$ except for that of the faintest one, which was $< 10^3 M_{\odot}$. The metallicity was comparable to a solar abundance and the age of the stars was $\sim 10^{6.8}$ yr. Their young stellar age meant that the star formation should have started after the gas was stripped from NGC 4388. This implied in situ condensation of the stripped gas. We also found that two star-forming regions were located near the leading edge of a filamentary dark cloud. The extinction of the filament was smaller than that derived from the Balmer decrement of the star-forming regions, implying that the dust in the filament would be locally dense around the star-forming regions.

Key words: galaxies: individual (NGC 4388) – H II regions – intergalactic medium

Online-only material: color figures

1. INTRODUCTION

In a cluster of galaxies, the galactic interstellar medium can be transferred into intergalactic space by various processes (Boselli & Gavazzi 2006, and references therein). The fate of the gas is, however, still not totally understood. Some of the gas would cool to form stars in intergalactic space; some would accrete back to the parent galaxy or to other galaxies in the cluster, and some would be heated to become hot plasma in the cluster.

If the gas is heated to $\sim 10^7$ K, it would be observed in X-rays. In fact, such X-ray tails associated with galaxies have been reported by many studies (e.g., Iwasawa et al. 2003; Wang et al. 2004; Machacek et al. 2005, 2006; Sun & Vikhlinin 2005; Sun et al. 2006, 2007, 2010; Fujita et al. 2006; Weżgowiec et al. 2011; Gu et al. 2013). The gas in the ionization–recombination balance phase would be observed in H α . The H α “tails” of galaxies have also been reported by many studies (e.g., Gavazzi et al. 2000, 2001; Yoshida et al. 2002; Sun et al. 2007, 2010; Yagi et al. 2007, 2010; Kenney et al. 2008; Smith et al. 2010; Fossati et al. 2012). If the gas remains cool, it should be observed in radio waves as H I tails (e.g., Oosterloo & van Gorkom 2005; Chung et al. 2007; Vollmer & Huchtmeier 2007) or molecular clouds (e.g., Vollmer et al. 2008, 2012). Several studies have presented models and simulations of the evolution of the gas in galaxies (e.g., Roediger et al. 2006; Roediger & Brüggén 2007, 2008; Kapferer et al. 2008; Tonnesen & Bryan 2012).

Note that the coexistence of X-ray, H α , and H I phases in a tail is rare (Roediger 2009; Sun et al. 2010). NGC 4388 in the Virgo Cluster is a rare example. From deep H α imaging, Yoshida et al. (2002) discovered a very extended ion-

ized region near the galaxy. The region was spectroscopically observed with the Faint Object Camera and Spectrograph (FOCAS; Kashikawa et al. 2002) at the Subaru Telescope (Yoshida et al. 2004). Yoshida et al. (2004) confirmed that the region had a recessional velocity comparable to that of NGC 4388. They also argued that the H α tail would have been made by ram-pressure stripping (Gunn & Gott 1972; Fujita & Nagashima 1999). Oosterloo & van Gorkom (2005) observed the region in H I 21 cm with the Westerbork Synthesis Radio Telescope and found that the H I tail extends to > 120 kpc from NGC 4388. Kenney et al. (2008) discovered another group of H α clouds between NGC 4438 to the east and M86 to the west. The clouds have ~ 0 km s $^{-1}$ heliocentric recessional velocity. Some part of the NGC 4438-M86 H α clouds overlap the extended gas of NGC 4388, but the difference in their heliocentric recessional velocities lets us distinguish between them. Recently, the association of X-ray gas near the tail of NGC 4388 was reported by Weżgowiec et al. (2011).

The origin of the tail of NGC 4388 has been discussed in several studies. Vollmer (2009) assumed that NGC 4388 is presently about 150 Myr after the closest approach to the cluster center, i.e., M87, and calculated the tangential velocities and the line-of-sight distance. They also discussed the possibility that the tail was formed by ram pressure from the intracluster medium (ICM) of the M86 group.

In the first paper of this series (Gu et al. 2013, hereafter Paper I), we reported that the H I gas accompanies the hot X-ray gas even ~ 100 kpc away from NGC 4388 and that both NGC 4388 and its H I tail lie in front of the M86 system. We compared the effect of the ICM of the M86 group and that of the Virgo Cluster (M87) and concluded that the tail could have

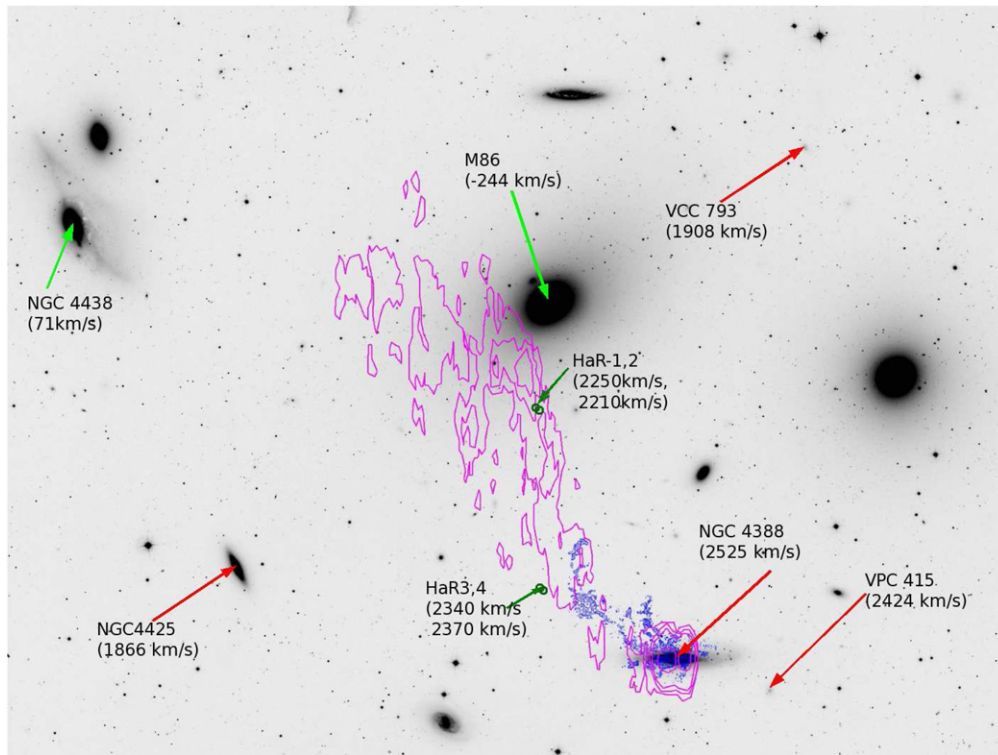


Figure 1. Virgo Cluster image in the SDSS r -band, coadded using the NASA/IPAC IRSA Montage service. North is up and east is to the left and the image size is 48×36 arcmin. The positions of the targets in this study (HaRs) are marked as open dark green circles and are indicated by arrows with labels. The velocities in the labels are the heliocentric recessional velocities. The blue contours near NGC 4388 show the $H\alpha$ tail extracted from the net $H\alpha$ data. The purple contours show the H I distribution by Oosterloo & van Gorkom (2005). Four high-velocity galaxies are indicated by red arrows. M86 and NGC 4438 are indicated by light green arrows. (A color version of this figure is available in the online journal.)

been made by ram-pressure stripping of the ICM of the Virgo Cluster.

In this paper, we report the identification of four intracluster/intergalactic star-forming regions in the Virgo Cluster, which are associated with the H I tail of NGC 4388. Intergalactic star formation in stripped gas from a galaxy has been reported by several authors (Owen et al. 2006; Sun et al. 2007, 2010; Cortese et al. 2007; Yoshida et al. 2008, 2012; Sivanandam et al. 2010; Smith et al. 2010; Hester et al. 2010; Fumagalli et al. 2011; Abramson et al. 2011; Fossati et al. 2012; Arrigoni Battaia et al. 2012; Boissier et al. 2012; Ohya & Hota 2013). Besides those in the tails, isolated star-forming regions in the Virgo Cluster were also reported (Gerhard et al. 2002; Arnaboldi et al. 2003; Cortese et al. 2003, 2004). Kronberger et al. (2008) and Kapferer et al. (2009) simulated the ram-pressure stripping of a galaxy and the star formation in the tail. Kronberger et al. (2008) showed that a significant fraction of stars would be formed in the tail and Kapferer et al. (2009) predicted that young stars would be detectable throughout the entire tail out to 400 kpc. Yamagami & Fujita (2011) showed that molecular clouds should be formed in the tail. This study will be directly compared with these model predictions.

The structure of this paper is as follows. In Section 2 and Appendix A, we describe the data we used, which include new spectroscopic observations. The spectroscopic data are analyzed in Section 3 and the physical parameters of four $H\alpha$ emitting regions are derived. The nature of the regions is discussed in Section 4 and summarized in Section 5. We adopt a distance to NGC 4388 and its tail of 16.7 Mpc (Yoshida et al. 2002). The distance modulus is $m - M = 31.11$ and one arcsec corresponds to 81.0 pc. The magnitude system is the AB system (Oke & Gunn 1983), unless otherwise noted.

2. DATA

2.1. Imaging Data

For a detailed analysis of the $H\alpha$ counterpart along the NGC 4388 tail, we retrieved data obtained with the Subaru Prime Focus Camera (Suprime-Cam; Miyazaki et al. 2002) around the H I tail in the N-A-L659 filter (Yoshida et al. 2002; Okamura et al. 2002; Hayashino et al. 2003, NA659 hereafter) and the R (W-C-RC)-band filter. The center wavelength of NA659 is 6600 Å and the FWHM is 100 Å, which corresponds to $H\alpha$ at a recessional velocity of $v = 1700 \pm 2300$ km s⁻¹. The NA659 imaging dataset was the same as that used in Yoshida et al. (2002), but we reprocessed it from the raw data for this paper. Recently, the region was observed much deeper in the R -band. We used the data for the continuum subtraction. Also, V (W-J-V), i (W-S-I+), and N-A-L503 (Yoshida et al. 2002; Okamura et al. 2002; Hayashino et al. 2003, NA503 hereafter) band data were available. The center wavelength of NA503 is 5020 Å and the FWHM is 100 Å. NA503 covered [O III]4959 and [O III]5007 at a recessional velocity of $v = 3680 \pm 3020$ and $v = 780 \pm 3000$ km s⁻¹ and did not cover $H\beta$ in the Virgo Cluster. The details of the Suprime-Cam data reduction are given in Appendix A.1. In Appendices A.2–A.6, the data in other wavelengths are described.

Based on a visual inspection, we selected two fields for spectroscopic observations. We call the four clumps of the $H\alpha$ -emitting regions HaR-1, 2, 3, and 4, from the north to the south (Figure 1). Their appearances are shown in Figures 2 and 3 and their coordinates are given in Table 1. HaR-2 consists of several sub-clumps. We call them HaR-2a, 2b, 2c, and 2d, from the north to the south, respectively. Their multiband magnitudes are given in Tables 2 and 3. It should be noted that there are

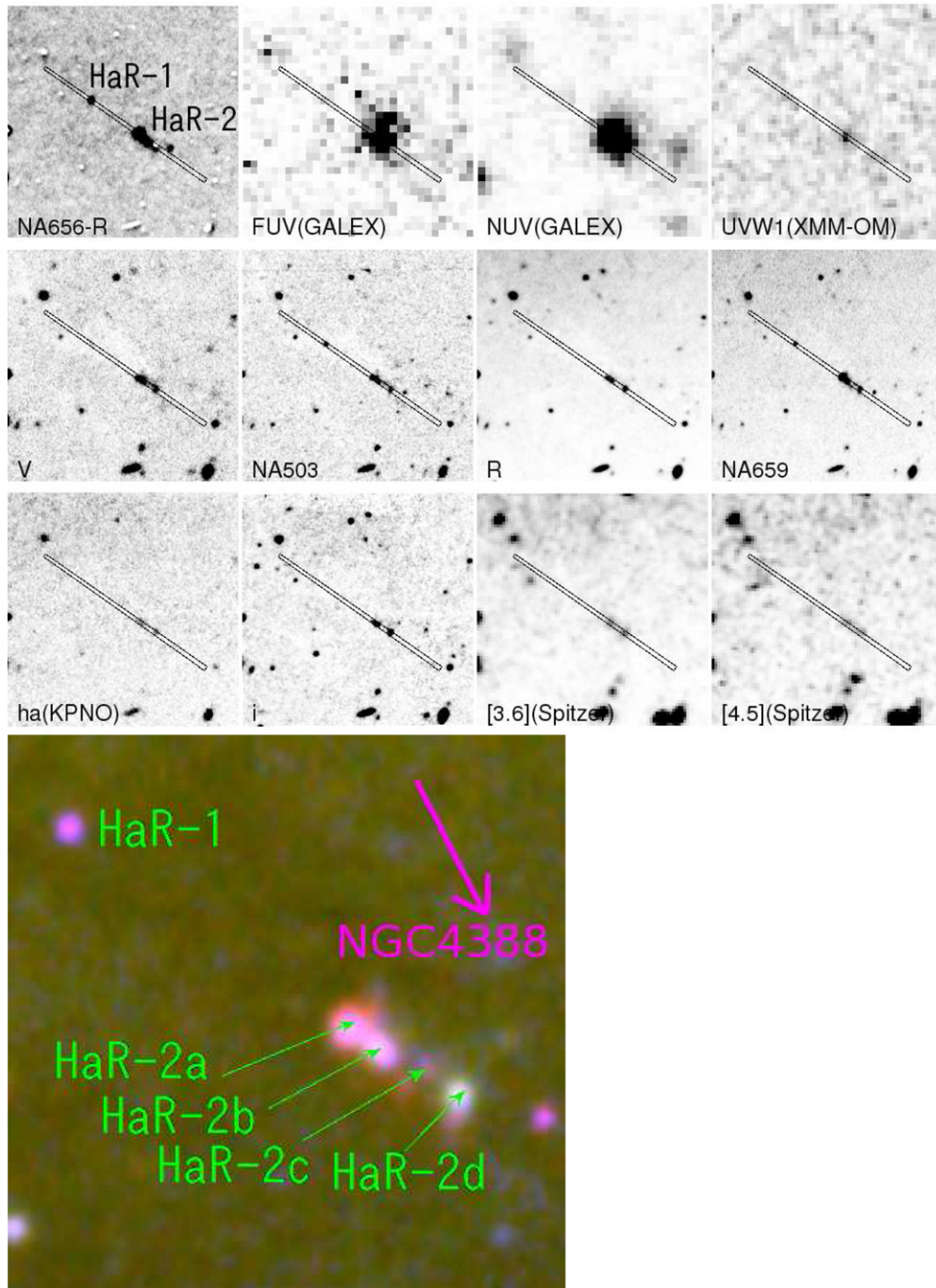


Figure 2. Top: postage stamp images of HaR-1 and HaR-2 in various wavelengths. North is up, east is to the left, and the image size is 50 arcsec on a side. The filter and telescope name are given in the lower left; the data are from Suprime-Cam/Subaru when no telescope name is given. The gray scale is arbitrary. The slit positions of the FOCAS observations are overlaid. Bottom: three color (NA659, *R*, NA503) composite images. North is up, east is to the left, and the image size is 20 arcsec on a side. The color scale is arbitrary. Magenta (red+blue) shows strong $H\alpha$ and $[O III]$ emission at the Virgo Cluster recessional velocity. The direction to the parent galaxy (NGC 4388) is shown by a magenta arrow at the top right.

(A color version of this figure is available in the online journal.)

other $H\alpha$ -emitting regions around the tail. The sampling of the $H\alpha$ -emitting regions in this study was not complete.

2.2. Spectroscopic Data

2.2.1. FOCAS Observations and Data Reduction

We carried out longslit spectroscopy in the two fields (HaR-1,2 and HaR-3,4) on 2013 March 3 (UT) with FOCAS (Kashikawa et al. 2002) attached to the Subaru Telescope. We

used a longslit 0.8 arcsec wide, and the 300B grism without order-cutting filters. The dispersion was $\sim 1.38 \text{ \AA pixel}^{-1}$. The pixel scale of the FOCAS data was 0.207 arcsec along the slit.

The data reduction was done in a standard manner: the overscan was subtracted and flat-fielded, cosmic rays were removed by a Python implementation of the LA Cosmic package (van Dokkum 2001),⁹ and the wavelength was calibrated using

⁹ http://obswww.unige.ch/~tewes/cosmics_dot_py/

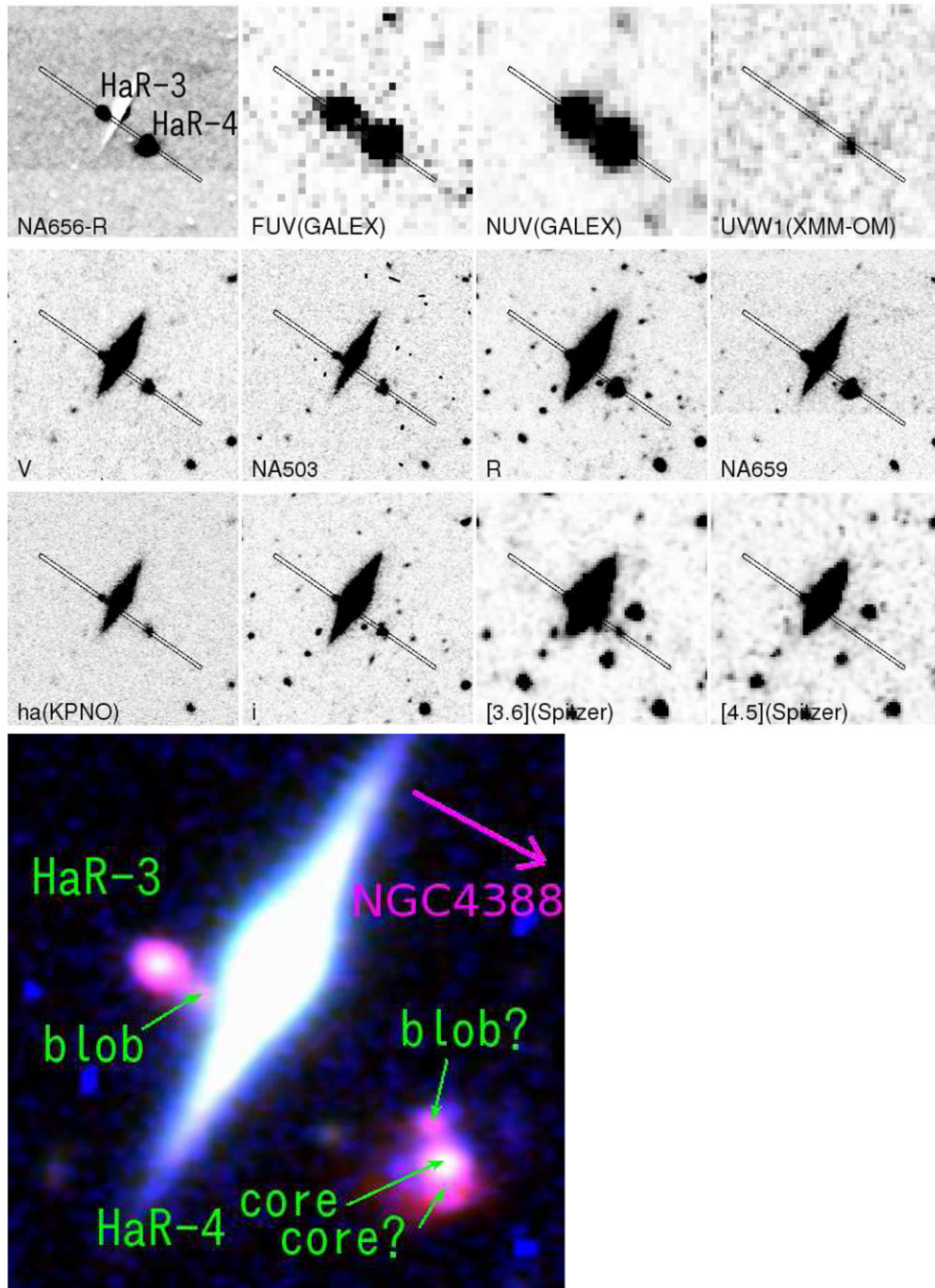


Figure 3. Same as Figure 2, but for HaR-3 and HaR-4. The apparent difference in the background color of the bottom panels of Figures 2 and 3 is due to the M86 stars behind the HaR-1,2 field.

(A color version of this figure is available in the online journal.)

sky emissions and a thorium-argon comparison lamp obtained during the observations. The measured instrumental profile was $\sim 9 \text{ \AA}$ FWHM. Then, the sky emissions and the absorption features of the sky background (mainly moonlights) were subtracted. The two-dimensional (2D) spectra around $H\beta$ and $H\alpha$ are shown in Figure 4.

Feige 67 was observed with a longslit 2.0 arcsec wide as a spectrophotometric standard. The calibrated spectrum was obtained from `calspec` in STScI.¹⁰ The atmospheric dispersion corrector at the Cassegrain focus was not available during the

observations and a wavelength-dependent positional shift of the target across the slit should have occurred. In our observing conditions, differential atmospheric dispersion was negligible for HaR-3,4, while a $\sim 13\%$ loss of flux may exist in the worst case for HaR-1,2. We therefore regard the $H\beta/H\alpha$ ratio of HaR-1 and 2 as possibly having suffered a 13% systematic error.

2.2.2. Spatial Distribution and Apertures

The spatial distribution of flux around $H\alpha$, $[\text{N II}]\lambda 6584$, and the continuum is shown in Figure 5. The $H\alpha$ and $[\text{N II}]$ fluxes are not only due to emission lines but also include continuum

¹⁰ http://ftp.stsci.edu/cdbs/current_calspec/

Table 1
Position of Targets

| Name | R.A. (J2000) | Decl. (J2000) |
|--------|--------------|---------------|
| HaR-1 | 12:26:14.63 | +12:51:46.4 |
| HaR-2a | 12:26:13.94 | +12:51:39.2 |
| HaR-2b | 12:26:13.87 | +12:51:38.6 |
| HaR-2c | 12:26:13.77 | +12:51:37.9 |
| HaR-2d | 12:26:13.68 | +12:51:36.8 |
| HaR-3 | 12:26:13.80 | +12:43:07.6 |
| HaR-4 | 12:26:13.09 | +12:43:00.4 |

flux. In HaR-1 and 4, $H\alpha$, $[N II]$, and the continuum profiles are similar. In HaR-3, the continuum shows a small gradient, which could be contamination from a neighboring galaxy at the position $x \sim 21$.

In HaR-2, the spatial profile was rather complicated. At $x \sim 24$, $H\alpha$ and $[N II]$ show peaks while the continuum does not. At $x \sim 25$, the continuum has a peak and $H\alpha$ and $[N II]$ show a bump. Around $x \sim 27$, $H\alpha$ and $[N II]$ show a small peak, but the continuum is ~ 0 . Then, a second peak in the continuum is seen at the slit position $x \sim 29$, where $H\alpha$ and $[N II]$ are not so strong as in the other part. We therefore divide the aperture of HaR-2 into four parts, which correspond to the clumps in Figure 2 (bottom). Then, spectra were extracted for the $H\alpha$ peaks with a Gaussian weight along the slit. The spectra are shown in Figure 6. In the figure, the wavelength dependence of the instrumental and atmospheric throughput is corrected, except for the possible slit loss. The neighboring galaxy between HaR-3 and 4 was found to be a background star-forming galaxy at $z = 0.118$.

2.2.3. Measurement of the Line Strengths

The strength of $H\alpha$, $[N II]6584$, $[S II]6717, 6731$, $[O III]5007$, and $H\beta$ were measured by Gaussian fitting. Over $6560 \text{ \AA} < \lambda < 6820 \text{ \AA}$, $H\alpha$, $[N II]$, and $[S II]$ were fit by a multivariate least-squares fitting. We assume that the background continuum is constant in the fitting region, that the redshift is the same for the lines, and that the FWHM of the lines is the same (dominated by the instrumental profile). The strength of $[N II]6548$ was fixed to be 1/3 of that of $[N II]6584$. The estimated redshifts are shown in Table 4. Over $4800 \text{ \AA} < \lambda < 5100 \text{ \AA}$, $H\beta$ and $[O III]5007$ are measured in the same way. $[O III]4959$ was assumed to be 1/3 of $[O III]5007$. At HaR-2c and HaR-2d, the lines are too weak and we could not fit well.

Since the seeing size was comparable to the slit width and the slit width was narrower than the spatial extent of the HaRs, the

Table 3
Narrowband Magnitudes after Galactic Extinction Correction

| Name | NA503 | NA659 | ha | ha4 |
|---------|------------------|------------------|------------------|------------------|
| HaR-1 | 24.14 ± 0.05 | 23.51 ± 0.05 | ... ^a | 23.22 ± 0.06 |
| HaR-2a | 23.74 ± 0.05 | ... ^b | 23.86 ± 0.14 | ... ^b |
| HaR-2b | 23.48 ± 0.06 | ... ^b | 23.25 ± 0.10 | ... ^b |
| HaR-2ab | ... | 21.06 ± 0.04 | 22.76 ± 0.08 | 21.09 ± 0.02 |
| HaR-2c | 24.34 ± 0.10 | ... ^a | ... ^a | ... ^a |
| HaR-2d | 23.83 ± 0.07 | 22.45 ± 0.04 | 23.52 ± 0.10 | 21.89 ± 0.05 |
| HaR-2 | 22.01 ± 0.05 | 20.80 ± 0.04 | 22.32 ± 0.07 | 20.67 ± 0.02 |
| HaR-3 | 22.20 ± 0.04 | 20.19 ± 0.04 | ... ^c | 20.19 ± 0.01 |
| HaR-4 | 21.72 ± 0.04 | 19.87 ± 0.04 | 21.39 ± 0.04 | 19.80 ± 0.01 |

Notes.

^a Non-detection.

^b Not resolved.

^c Heavily blended with a background galaxy.

Table 4
Recessional Velocity in the Heliocentric Reference Frame and Projected Distance from NGC 4388

| Name | z | v (km s^{-1}) | d (kpc) |
|--------|---------|-------------------------------|--------------|
| HaR-1 | 0.00749 | 2.25×10^3 | 67.1 |
| HaR-2a | 0.00737 | 2.21×10^3 | 66.2 |
| HaR-2b | 0.00737 | 2.21×10^3 | 66.1 |
| HaR-2c | 0.00736 | 2.21×10^3 | 66.0 |
| HaR-2d | 0.00731 | 2.19×10^3 | 65.9 |
| HaR-3 | 0.00780 | 2.34×10^3 | 35.9 |
| HaR-4 | 0.00789 | 2.37×10^3 | 34.9 |

flux value from the spectra has little physical meaning but the flux ratios are meaningful. The ratios are shown in Table 5. The error of each parameter was estimated by a residual bootstrap method with 1000 realizations, except for $H\alpha/H\beta$. The error of $H\alpha/H\beta$ was estimated from the error of the $H\alpha$ flux and that of the $H\beta$ flux by residual bootstrapping, assuming that their errors were independent. For HaR-1 and HaR-2, a 13% error due to a possible differential atmospheric dispersion effect was also included.

In Figure 7, diagnostic line ratio plots are shown. All the regions have a line ratio similar to an H II region. Moreover, $[O I]6300$ was not detected in any of the regions and a possible contribution of shock, as seen in $H\alpha$ knots in Yoshida et al. (2004), are negligible in our targets. Note that $[O I]6300$ of the HaRs is not affected by the atmospheric $[O I]6300$ or $[O I]6363$, because of the redshift.

Table 2
Broadband Magnitudes after Galactic Extinction Correction

| Name | FUV | NUV | V | R | i | 3.6 μm | 4.5 μm |
|---------|------------------|------------------|--------------------|--------------------|--------------------|-------------------|-------------------|
| HaR-1 | $>24.4^a$ | 24.7 ± 0.2 | $>26.43^b$ | 25.73 ± 0.09 | $>26.3^b$ | $>24.3^b$ | $>24.1^b$ |
| HaR-2ab | ... ^c | ... ^c | 22.76 ± 0.04 | 22.59 ± 0.04 | 22.72 ± 0.04 | 22.1 ± 0.1 | 23.0 ± 0.3 |
| HaR-2d | ... ^c | ... ^c | 22.86 ± 0.06 | 22.68 ± 0.04 | 22.52 ± 0.04 | 22.2 ± 0.2 | 23.3 ± 0.4 |
| HaR-2 | 21.88 ± 0.09 | 21.85 ± 0.04 | 22.06 ± 0.07 | 21.88 ± 0.04 | 21.86 ± 0.05 | 21.5 | 22.4 |
| HaR-3 | 21.80 ± 0.09 | 21.86 ± 0.04 | 22.31 ± 0.05^d | 21.91 ± 0.04^d | 22.00 ± 0.06^d | $>21.4^e$ | $>21.7^e$ |
| HaR-4 | 21.24 ± 0.07 | 21.18 ± 0.03 | 21.53 ± 0.04 | 21.08 ± 0.04 | 21.76 ± 0.04 | 22.0 ± 0.1 | 22.9 ± 0.3 |

Notes.

^a No object shape, but has a positive flux in an aperture.

^b 1σ limiting magnitude.

^c Not resolved.

^d $\phi = 2$ arcsec aperture photometry.

^e Twice the semi-circular aperture flux.

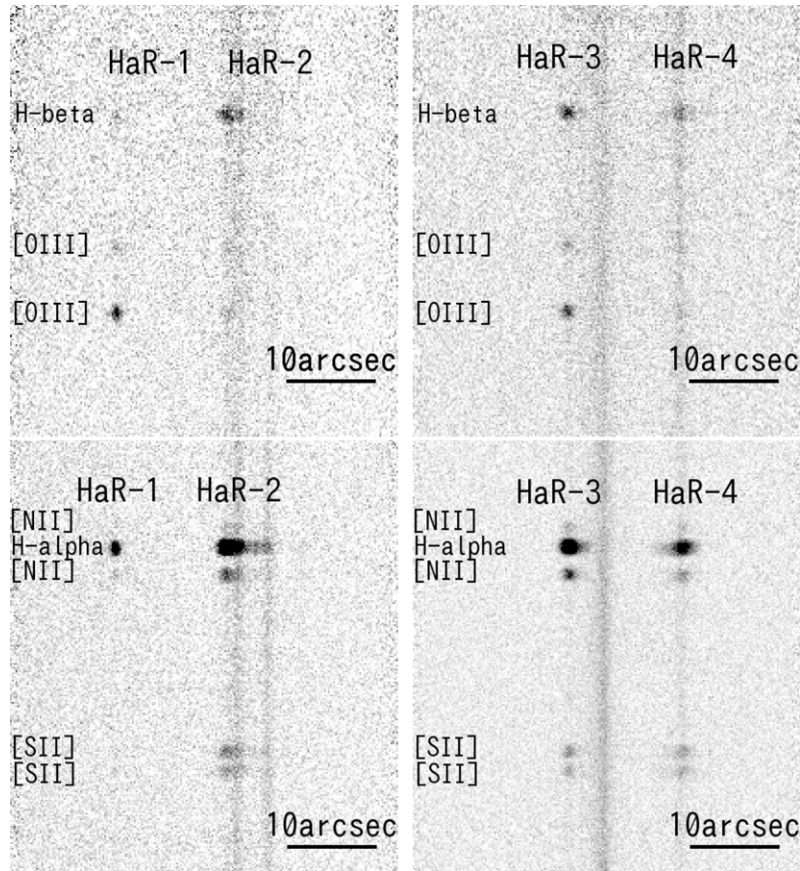


Figure 4. Cutouts of FOCAS 2D spectra after sky subtraction. The top panels show the spectra around $H\beta$ and $[O\text{ III}]$. The bottom panels show the spectra around $H\alpha$, $[N\text{ II}]$, and $[S\text{ II}]$.

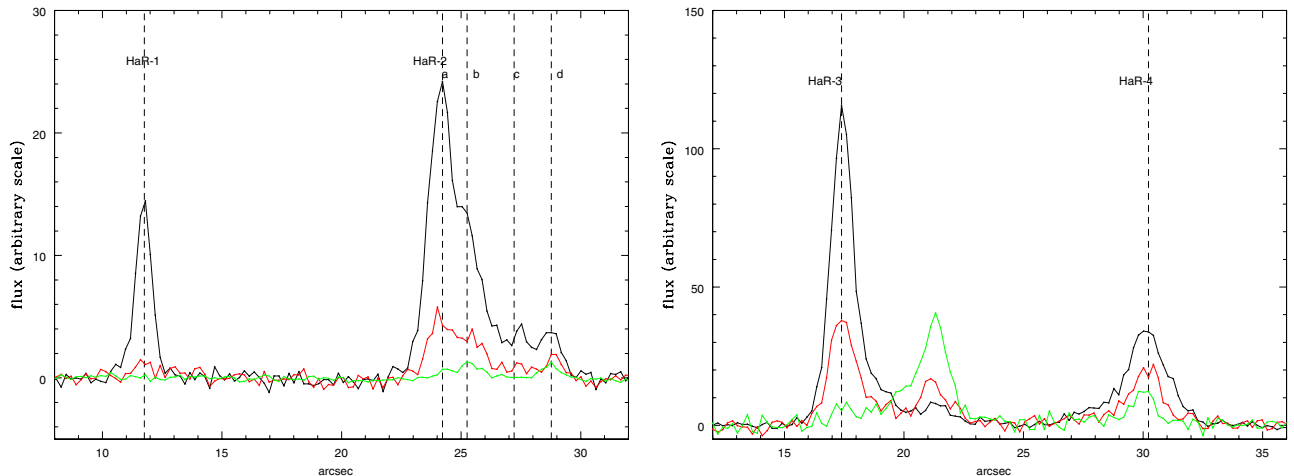


Figure 5. Spatial distribution of $H\alpha$ (black), $[N\text{ II}]6584$ (red), and the continuum ($6654\text{--}6750\text{ \AA}$ in the observed frame; green). $H\alpha$ and $[N\text{ II}]$ include continuum flux. $[N\text{ II}]$ is scaled $\times 2$ and the continuum is scaled $\times 5$ for comparison with $H\alpha$. The center of each aperture is shown as a vertical broken line. The origin of the spatial coordinate (\times) and the flux units are arbitrary. Top: HaR-1,2. HaR-2 shows several different sub-regions. Bottom: HaR-3,4. The continuum peak at $x = 21$ arcsec is a background galaxy.

(A color version of this figure is available in the online journal.)

3. RESULTS

3.1. Redshift and Position

The HaRs have large ($>2000\text{ km s}^{-1}$) recessional velocities. The recessional velocity of NGC 4388 is also large, 2524 km s^{-1} (Lu et al. 1993), and that of the H I tail is $2000\text{--}2550\text{ km s}^{-1}$ (Oosterloo & van Gorkom 2005). As the recessional velocity of the Virgo Cluster is 1079 km s^{-1} (Ebeling et al. 1998), the peculiar velocity of NGC 4388 and its tail is $>900\text{ km s}^{-1}$.

In the 48×36 arcmin region shown in Figure 1, the number of galaxies that have recessional velocities larger than 1500 km s^{-1} in NASA/IPAC Extragalactic Database (NED) is seven. Two of them, AGC 226080 and VCC 956, have an H I redshift only. As the beam of the H I observation is large enough (3.3×3.8 arcmin; Giovanelli et al. 2007) to include the H I tail of NGC 4388, the high velocity could be measured due to an accidental overlap with the tail. The recessional velocity of VCC896 is uncertain, since it is inconsistent among Conselice et al. (2001), the Sloan

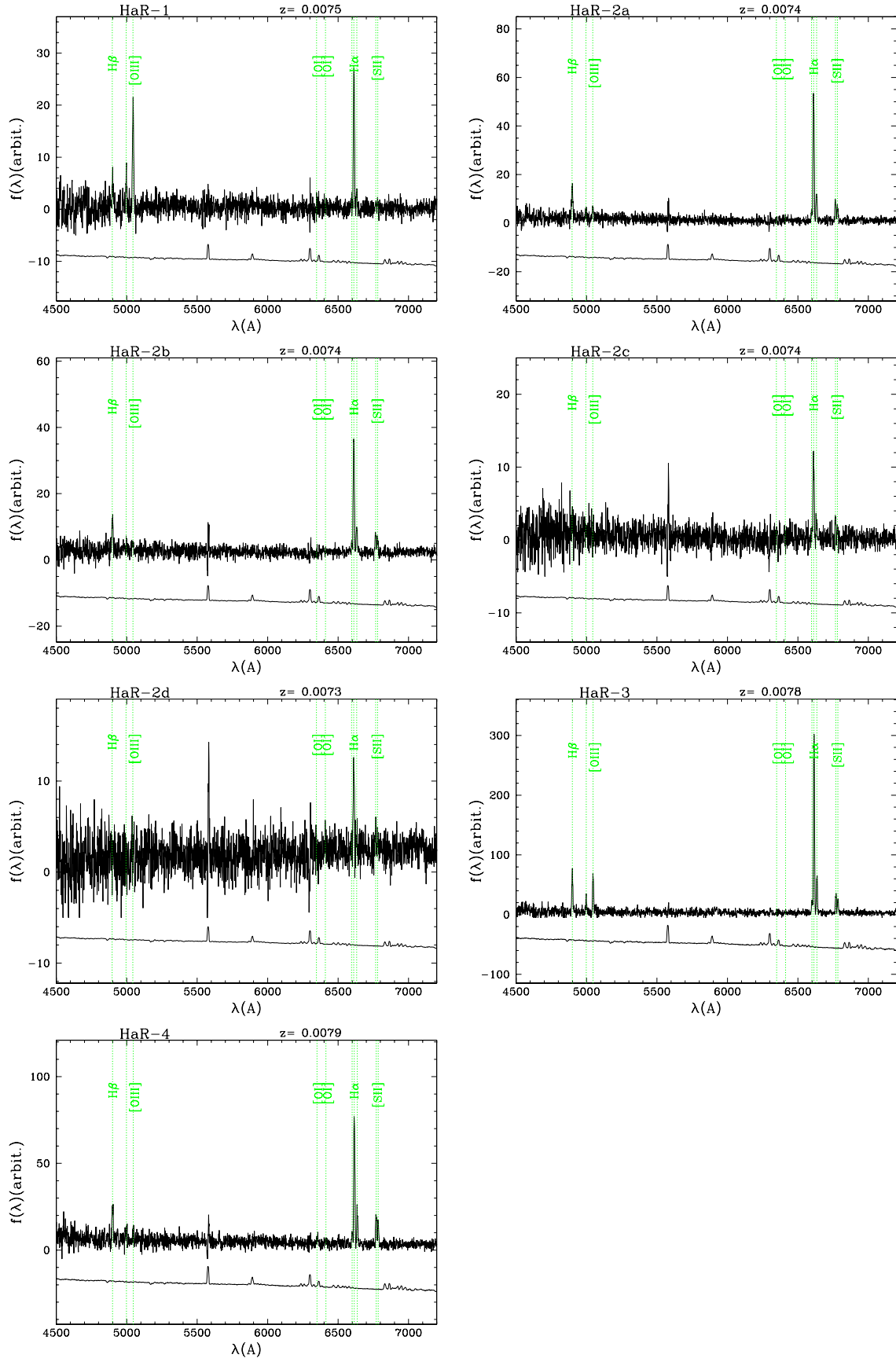


Figure 6. Spectra of H α -emitting regions. From left to right and top to bottom, spectra of HaR-1, 2a, 2b, 2c, 2d, 3, and 4 are shown. The green lines indicate the position of emission lines at the redshift in Table 4. The subtracted sky spectrum (scaled) is shown below each spectrum for reference. Wavelengths are in the rest frame.

(A color version of this figure is available in the online journal.)

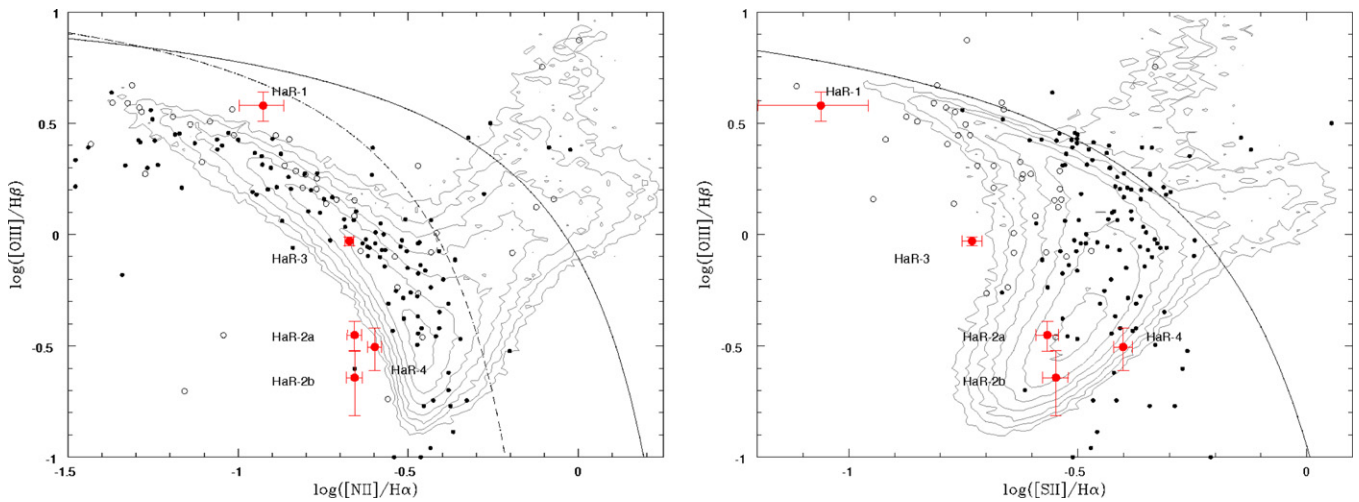


Figure 7. Line ratio plot. The large, filled circles with error bars are the data from this study. The solid and broken curves are the demarcation between H II regions and active galactic nuclei by Kewley et al. (2001) and Kauffmann et al. (2003), respectively. Filled dots represent nearby field galaxies (Jansen et al. 2000) and open dots represent blue compact galaxies from Kong et al. (2002). The contours show the distribution of SDSS galaxies in the MPA-JHU DR7 release of spectrum measurements. The data whose emission-line signal-to-noise ratios are larger than 3 are used and the number of galaxies are 4.0×10^5 and 3.5×10^5 for $[\text{N II}]/\text{H}\alpha$ vs. $[\text{O III}]/\text{H}\beta$ and $[\text{S II}]/\text{H}\alpha$, respectively. The contour interval is a factor of $10^{1/4}$.

(A color version of this figure is available in the online journal.)

Table 5
Line Ratios

| Name | $[\text{N II}]/\text{H}\alpha$ | $[\text{S II}]/\text{H}\alpha$ | $[\text{S II}]/[\text{N II}]$ | $[\text{O III}]/\text{H}\beta$ | $\text{H}\alpha/\text{H}\beta$ |
|--------|--------------------------------|--------------------------------|-------------------------------|--------------------------------|--------------------------------|
| HaR-1 | 0.12 ± 0.02 | 0.09 ± 0.02 | 0.88 ± 0.49 | 3.79 ± 0.57 | 5.4 ± 0.8^a |
| HaR-2a | 0.22 ± 0.01 | 0.27 ± 0.02 | 1.45 ± 0.17 | 0.35 ± 0.05 | 4.0 ± 0.3^a |
| HaR-2b | 0.22 ± 0.01 | 0.28 ± 0.02 | 1.34 ± 0.17 | 0.23 ± 0.07 | 3.7 ± 0.4^a |
| HaR-2c | 0.22 ± 0.04 | 0.35 ± 0.05 | 2.39 ± 0.92 | 0.07 ± 0.25 | 6.1 ± 3.0^a |
| HaR-2d | 0.17 ± 0.06 | 0.37 ± 0.08 | 1.56 ± 0.67 | ... ^b | $>4.4^{a,c}$ |
| HaR-3 | 0.22 ± 0.01 | 0.19 ± 0.01 | 1.44 ± 0.14 | 0.93 ± 0.04 | 4.4 ± 0.2 |
| HaR-4 | 0.25 ± 0.01 | 0.40 ± 0.02 | 1.29 ± 0.11 | 0.31 ± 0.07 | 3.7 ± 0.3 |

Notes.

^a Including 13% error due to possible differential atmospheric dispersion effects.

^b $[\text{O III}]$ and $\text{H}\beta$ non-detection.

^c From the upper limit of $\text{H}\beta$.

Digital Sky Survey Data Release 7 (SDSS-II DR7; Abazajian et al. 2009)¹¹ and SDSS-III DR9 (Ahn et al. 2012).¹² The remaining four have optical spectroscopic redshifts that are consistent among the literature. We marked the four in Figure 1. The HaRs are very likely to be associated with the H I tail of NGC 4388 because of the large recessional velocity and their position; HaR-1 and HaR-2 overlap the H I and HaR-3 and HaR-4 lie near the contour edge (Figure 1); the nearest galaxy with a large recessional velocity is NGC 4388.

3.2. Size and Morphology

HaR-1 is a point source and was only detected in narrowband data. It is marginally detected in the near-ultraviolet (NUV) and in optical broadbands that include strong emission. Since the seeing in the NA659 filter was about 0.75 arcsec, which corresponds to 60 pc, the size of HaR-1 would be smaller than 60 pc.

HaR-2 shows a blobby and elongated appearance. Its size is 530×210 pc. HaR-2ab and HaR-2d were recognized separately in optical and infrared images, while they were merged in UV

images due to the 6 arcsec resolution of the *Galaxy Evolution Explorer* (GALEX).

HaR-3 had a slightly elongated shape toward HaR-4 and showed a sign of a tail with a blob. The tail was contaminated by the light from the neighboring background galaxy and the length of the tail was uncertain. The size of HaR-3, including the tail, was $>300 \times 180$ pc.

HaR-4 showed a possible multi-core or elongated core surrounded by a blob and extended plume (Figure 3). The size, including the plume, was 380×360 pc. It is interesting that HaR-3 had an H α tail toward NGC 4388. In HaR-2ab and HaR-4, the tail/plume was on the far side of NGC 4388. The distance between HaR-3 and HaR-4 is 13 arcsec (1 kpc) and the difference in the recessional velocities of HaR-3 and 4 is 30 km s^{-1} . Even if the masses of HaR-3 and 4 are $\sim 10^6 M_{\odot}$, they would not be bound gravitationally.

3.3. Internal Extinction and H α Luminosity

Internal extinction was estimated from the Balmer decrement $\text{H}\beta/\text{H}\alpha$ in our FOCAS spectra. We adopted the formula by Calzetti et al. (1994),

$$E(B - V) \simeq 0.935 \ln((\text{H}\alpha/\text{H}\beta)/2.88). \quad (1)$$

The estimated internal extinction is listed in Table 6.

¹¹ <http://cas.sdss.org/dr7/en/>

¹² <http://skyserver.sdss3.org/dr9/>

Table 6
H α Luminosity

| Name | m (NA659) | $E(B - V)$ | $\log(f(\text{H}\alpha))$ ($\text{erg s}^{-1} \text{cm}^{-2}$) | $\log(L(\text{H}\alpha))$ (erg s^{-1}) |
|--------|--------------------|------------------------|---|--|
| HaR-1 | 23.51 ± 0.05 | $0.59^{+0.13}_{-0.15}$ | $-16.63^{+0.15}_{-0.13}$ | $35.89^{+0.15}_{-0.13}$ |
| HaR-2a | 21.06 ± 0.04^a | 0.31 ± 0.07 | -15.45 ± 0.07 | 37.07 ± 0.07 |
| HaR-2b | ... | $0.23^{+0.10}_{-0.11}$ | ... | ... |
| HaR-2c | ... | $0.3^{+0.2}_{-0.3}$ | ... | ... |
| HaR-2d | 22.45 ± 0.04^b | >0.4 | >-16.53 | >35.99 |
| HaR-2 | ... | ... | ... | >37.10 |
| HaR-3 | 20.19 ± 0.04 | 0.40 ± 0.04 | -15.17 ± 0.04 | 37.35 ± 0.04 |
| HaR-4 | 19.87 ± 0.04 | $0.23^{+0.07}_{-0.08}$ | $-14.99^{+0.08}_{-0.07}$ | $37.53^{+0.08}_{-0.07}$ |

Notes.^a HaR-2a magnitude and flux includes HaR-2b and part of the 2c region.^b HaR-2d magnitude and flux includes part of the 2c region.

In our observations, the seeing was comparable to the slit width. We therefore did not try an absolute spectrophotometric calibration from the spectra only. Instead, the spectra were used to convert the NA659 magnitude to the total flux of H α . The extinction-corrected H α luminosities are given in Table 6.

3.4. Metallicity

Kewley & Dopita (2002) presented model curves to estimate the oxygen abundance ($\log(\text{O}/\text{H})+12$) using several combinations of emission lines with various values of the ionization parameter (q). We can use $[\text{N II}]/[\text{S II}]$, $[\text{N II}]/\text{H}\alpha$, and $[\text{N II}]/[\text{O III}]$ to estimate the metallicity. $[\text{N II}]/[\text{O III}]$ was corrected for the internal extinction using $\text{H}\beta/\text{H}\alpha$ and other two ratios were not corrected. q was also estimated from the curves.

From the fitting, the metallicity of the regions was estimated as $\log(\text{O}/\text{H})+12 \sim 8.6\text{--}8.7$, comparable to a solar abundance (Grevesse et al. 2010). Yoshida et al. (2004) reported that the metallicity of H α -emitting filaments near NGC 4388 was almost solar. Their ionization parameters correspond to $\log(U) = -2.6, -3.5, -3.2$, and -3.5 , for HaR-1, 2a, 3, and 4, respectively, where U is the ratio of the ionization photon density to the electron density. Since $\log(U)$ decreases with age in H II regions, a relatively large value for HaR-1 implies that HaR-1 would be younger.

3.5. Electron Density

From Figure 5.8 of Osterbrock & Ferland (2006), O'Dell et al. (2013) derived the formula to estimate the electron density (n_e):

$$\log(n_e) = 4.705 - 1.9875 ([\text{S II}]6716/[\text{S II}]6731), \quad (2)$$

which was applicable in the regime $0.65 < [\text{S II}]6716/[\text{S II}]6731 < 1.3$. In this study, the error of $[\text{S II}]6717/[\text{S II}]6731$ was large and all regions except for HaR-1 were consistent with $n_e \lesssim 10^2 \text{ cm}^{-3}$. HaR-1 may have a higher electron density, $n_e \sim 10^3 \text{ cm}^{-3}$.

3.6. Mass and Age Estimation

We calculated model magnitudes and H α fluxes at different ages and compared them with the observations. The details of the model are given in Appendix B. We plotted the model age versus the model mass to reproduce the observations in Figure 8. The abscissa is the logarithmic age from the burst and the ordinate is the required stellar mass of the HaR to reproduce

the observed magnitude/luminosity at each age. Because the time evolution of the H α luminosity and the UV, optical, and mid-infrared magnitudes are different, the crossing point of the tracks will indicate the stellar mass and the age.

H α , IR, and UV were comparable around $\log(T) = 6.8$ and $\log(\text{mass}) = 4.3$ in the Geneva model for HaR-2, HaR-3, and HaR-4, while i is offset by ~ 0.4 dex, which corresponds to ~ 1 mag and a factor of ~ 2.5 . Although the consistency in the Padova model was not as good as that of the Geneva model, the best-fit mass and age were comparable.

The disagreement of the estimated mass and age among the data might be explained partly by the difference in aperture sizes. Since the UV resolution was the poorest, it required the largest aperture ($r = 6$ arcsec), which may have included contaminants, thereby making the observed luminosity larger and shifting the lines in Figure 8 upward. However, the infrared (IR) had a smaller aperture ($r = 3$ arcsec) than the UV and H α was based on NA659 photometry, which used an aperture of $2.5 \times$ Kron radius (r_K). $2.5r_K$ was 2 ± 0.3 arcsec in the data and therefore was the smallest aperture because of the best seeing. Suprime-Cam i -band and Kitt Peak National Observatory (KPNO) mosaic h -band fluxes were also measured in an aperture of $2.5r_K$ radius, which was 2–3 arcsec. Nevertheless, the H α , UV, and IR data showed good agreement, while the i -band and KPNO h -band showed an offset in HaR-2 and HaR-3. As the i -band magnitude of Suprime-Cam was comparable to the SDSS photometry for HaR-4, which was based on the Petrosian radius, and the KPNO photometry of the h -band showed a similar trend, the disagreement could not be caused by photometric error.

The disagreement also could come from model uncertainties and adopted assumptions, such as initial mass function (IMF), instantaneous star formation, and/or the dust extinction model. A possible model is to divide the region into several sub-regions and to assume different extinctions. For example, if some part has a large extinction, the UV is suppressed and the optical and IR fluxes could be larger relative to UV and H α . In fact, HaR-2 consisted of sub-clumps with various extinctions. Although we can consider various star formation histories and models, such an analysis is beyond the scope of this study. We do not further tune the star formation histories and the models.

In Figure 8, HaR-1 shows the large disagreement among the data. Since HaR-1 would have a smaller mass, which was expected from its fainter i -band magnitude, it may have suffered from stochastic IMF effects (e.g., Koda et al. 2012).

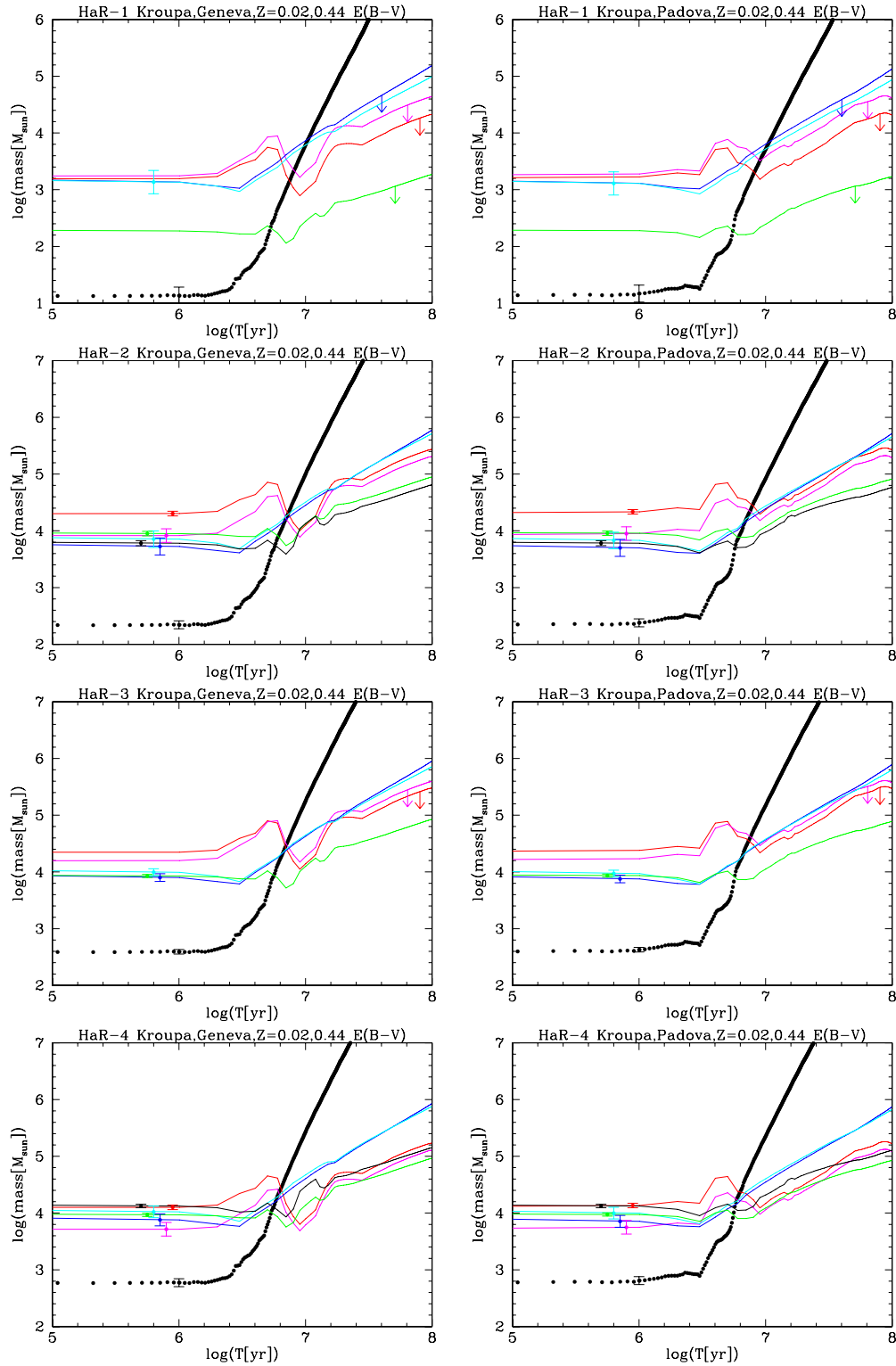


Figure 8. Age and mass estimation using the STARBURST99 model. The combinations of the age(T) and mass to reproduce the observed $H\alpha$ luminosity ($L(H\alpha)$) are shown as black dots. Solid lines correspond to the combination to reproduce the observed magnitudes in FUV (blue), NUV (cyan), i (green), KPNO ha (black), $3.6\ \mu\text{m}$ (red), and $4.5\ \mu\text{m}$ (red). Detailed explanation is given in Appendix B. Those on the left are Geneva tracks and those on the right are Padova tracks. The arrows indicate that the quantity is an upper limit. The error bars are shown around $\log(T) = 6$. The error includes the photometric error and the error from the $E(B - V)$ estimation and is the same at all T .

(A color version of this figure is available in the online journal.)

As shown in Table 4, HaR-1 and 2 are 66 kpc away from NGC 4388 and HaR-3 and 4 are 35 kpc away from NGC 4388. Oosterloo & van Gorkom (2005) and Vollmer (2009) assumed that the age of the H I cloud is ~ 200 Myr and estimated the

projected velocity of NGC 4388 to the cloud to be $500\ \text{km s}^{-1}$. If we adopt this value as the velocity of the HaRs relative to NGC 4388, it should take 130 Myr (HaR-1 and 2) and 70 Myr (HaR-3 and 4) to reach the corresponding distances. Since the

timescales are longer than the stellar age estimated above, the result suggests that the star formation in HaRs began after the gas left the host galaxy. This is consistent with the prediction by Yamagami & Fujita (2011).

4. DISCUSSION

4.1. Comparison with Previous Studies

Table 7 summarizes the literature concerning a stripped tail in nearby clusters of galaxies. Since the environment and physical condition of the tails (the ambient gas temperature and density, the relative velocity, the density of the tail, etc.) vary, we cannot compare them directly. We can at least say that HaR-1 and 2 are the most distant star-forming regions and HaR-1 may be the least massive region. Also, we can say that $10^{4-5} M_{\odot}$ and $\sim 10^7$ yr star-forming regions in a stripped tail are not peculiar properties.

The ages of the regions in Fumagalli et al. (2011) are substantially larger than the others, probably because a different model of the star formation history was adopted. The mass estimation is not affected by the different star formation history. The detection of the star-forming regions was based on H α and/or UV emission and therefore the sampling should be biased toward younger ages.

4.2. Comparison with the H I Distribution and the Recessional Velocity

The detailed heliocentric velocity distributions of H I¹³ showed that the intensity of H I in the HaR-1,2 fields has a wide peak around a recessional velocity of ~ 2240 km s⁻¹ (intensity-weighted mean) with a width of ~ 150 km s⁻¹. HaR-1 and 2 are just on the peak. This means that the star-forming regions have only small peculiar velocities relative to the ambient H I cloud along the line of sight. Meanwhile, H I in the HaR-3,4 fields showed no significant peak. Since the star formation in the stripped tail is thought to occur in the highest-density regions (Kapferer et al. 2009), it is puzzling that the H I flux in the HaR-3,4 fields is low.

As we reported in Paper I, the tail of NGC 4388 is accompanied by relatively cool X-ray gas and the distribution of X-ray emission showed a marginal enhancement downstream of HaR-3,4. The H I gas around HaR-3 and 4 might already have evaporated, except for the densest region. Another possibility is that such dense clouds are less affected by ram pressure and left behind the H I gas (Yamagami & Fujita 2011).

4.3. Positional Offset of H α and Stars and a Dark Cloud around HaR-1 and HaR-2

The 2D spectrum and the slit profile of HaR-2 (Figures 4 and 5) shows that the H α -strong region (HaR-2a) appears to the left of the continuum regions (HaR-2b). They resemble the fireballs found in the ram-pressure stripped tail in RB199 in the Coma cluster (Yoshida et al. 2008, 2012).

If the gas cloud (HaR-2a, 2c) is now free from the ram pressure, the gas and stars would move similarly. On the other hand, because the ram pressure affects the stars and gas differently, it would cause differential movement between the gas and the stars. The positional shift between the gas and the stars implies that ram-pressure deceleration is still working here,

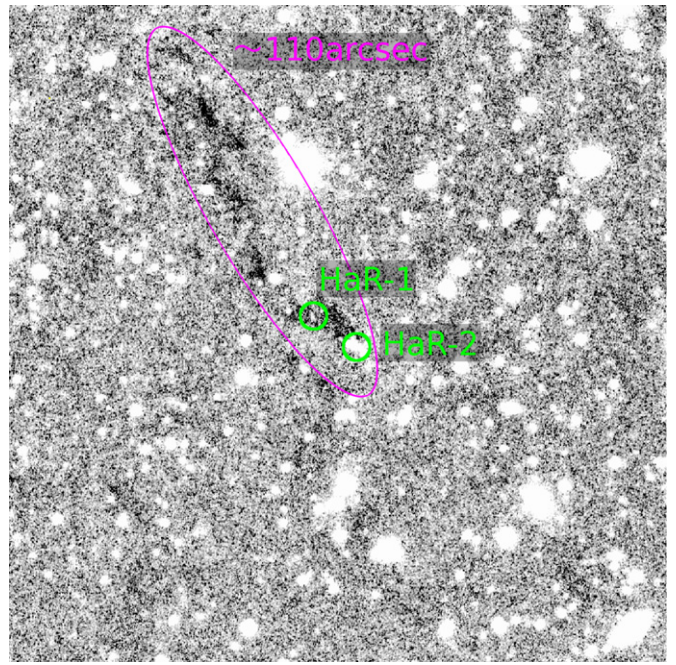


Figure 9. Wider view around HaR-1 and 2 in the V-band with a higher contrast and the grayscale inverted from Figure 2. The magenta ellipse indicates the winding dark filament. HaR-2 is at the tip of the filament, whose length is about 110 arcsec (~ 9 kpc).

(A color version of this figure is available in the online journal.)

66 kpc away from the host galaxy. Another possible explanation for the offset is that the gas has been consumed from the leading edge of the cloud and that the star formation is propagated to the following regions.

In HaR-4, a plume also exists on the other side of the parent galaxy. In HaR-3, however, the tail appears on the side of the parent galaxy. The direction was coincident with the direction to HaR-4. The projected distance between HaR-3 and HaR-4 was about 1.0 kpc and the difference of their recessional velocities was 30 km s⁻¹. If their masses are $\sim 10^5 M_{\odot}$, the velocity difference is so large that they cannot be gravitationally bound. If HaR-3 and HaR-4 had experienced an encounter in the past, it means that such a small-scale motion existed in the tail.

Illuminated by the stars of the M86 envelope, a dark filamentary cloud was recognized around HaR-1 and HaR-2. A high contrast V-band image is shown as Figure 9. In the optical bands of Figure 2, the cloud was also recognized. The dark cloud shows an elongated and twisted shape. The length is ~ 110 arcsec (7 kpc) and the width is ~ 7 arcsec (600 pc) around HaR-2.

It is uncertain whether the dark cloud is associated with the NGC 4388 tail, is an accidental overlap of a dark cloud of M86, or even if it is another dark cloud. However, as filaments of the dark cloud are only recognized along the H I tail of NGC 4388, it is likely that the dark cloud is associated with the NGC 4388 H I tail. These filaments of the dark cloud do not show any H α emitting regions except those with HaR-1 and HaR-2. As there are only a few star-forming regions along the tail, it is unlikely that the dust was created in the tail; the origin of the dust should be NGC 4388. It implies that the dust was affected by the ram pressure. The ram-pressure stripping of dust from disk of galaxies in the Virgo Cluster has been suggested by several authors; NGC 4402 by Crowl et al. (2005), NGC 4438 by Cortese et al. (2010a), and NGC 4330

¹³ Provided by Dr. J. van Gorkom. The beam of the data was elongated from the north to the south: 77 arcsec in declination and 24.5 arcsec in right ascension.

Table 7
Star-forming Regions in a Ram-pressure-stripped Tail of a Galaxy

| Cluster | Galaxy | Proj. Dist. (kpc) ^a | log (mass(M_{\odot})) | log (age(yr)) | Reference |
|---------|----------|-----------------------------------|------------------------------|------------------|--------------------------------|
| A3627 | 137-001 | 0–40 | ... | ... | Sun et al. (2010) |
| Coma | RB199 | 23–35 | 5.8–7.1 | ~8 | Yoshida et al. (2008) |
| | IC 4040 | 1.1–48 | ... | ~8 | Yoshida et al. (2012) |
| | NGC 4848 | 22–35 | ... | ... | Fossati et al. (2012) |
| Virgo | IC 3418 | 10–17 | 4.5–5.6 | 8.2–9.1 | Fumagalli et al. (2011) |
| | | ~14 | 4 | 6.8(7.2/7.3) | Ohya & Hota (2013) |
| | NGC 4330 | <9 | 3.3–6.3 | (< 7)–8.5 | Abramson et al. (2011) |
| | VCC 1249 | 5–12 | 3.8–4.3 | 6.6–7.3 | Arrigoni Battaia et al. (2012) |
| | NGC 4388 | 66 | <3 | <7 | this study (HaR-1) |
| | | 35,66 | 4–4.5 | 6.7–6.9 | this study (HaR-2,3,4) |

Note. ^a Projected distance from the parent galaxy.

by Abramson et al. (2011). Cortese et al. (2010b) studied H I-deficient galaxies in the Virgo Cluster and found that dust is stripped in the cluster environment, as well as the gas. Yoshida et al. (2012) demonstrated the coincidence of the ram-pressure stripping of H I, H α , and the dust in IC 4040. The elongated and twisted shape of the dark cloud downstream of HaR-1 and HaR-2 may also be explained as a result of the ram pressure that is still effective around the regions.

In Paper I, we showed evidence that M86 is more distant than the NGC 4388 tail. The total extinction of the cloud was estimated by assuming that the background M86 light was smooth. The estimated extinction at a region between HaR-1 and HaR-2 was ~15% and ~10% in the V-band and in the R-band, respectively, corresponding to $E(B - V) \sim 0.05$. As the $E(B - V)$ estimated from the Balmer decrement in HaR-1 is much larger ($E(B - V) = 0.59^{+0.13}_{-0.15}$), we suggest that the dust in the dark filament is locally dense around the star-forming regions.

4.4. Star Formation in the Clouds

Based on the argument of Yamagami & Fujita (2011), we discuss the star formation in the molecular clouds that later shine as the observed H α -emitting regions. Elmegreen & Efremov (1997) derived the relation between the mass of a cloud M_c and the star formation efficiency ϵ when the cloud is under a pressure P_c . We estimate in Paper I that the ram pressure on NGC 4388 and the clouds should be $P_{\text{ram}} \sim 4 \times 10^{-12} \text{ dyn cm}^{-2}$. In Section 3.6, we found that the total mass of stars in each H α emitting region is $M_* \sim 10^4\text{--}10^{4.5} M_{\odot}$. Assuming that $P_c = P_{\text{ram}}$, the mass of the molecular cloud before the stars were born is $M_c \sim 10^{5.5} M_{\odot}$ because $\epsilon \sim 0.1$ (the lower part of Figure 4 in Elmegreen & Efremov 1997). For this mass and pressure, the timescale of star formation in the cloud is $\tau_{\text{form}} \sim 10^7 \text{ yr}$ (the upper part of Figure 4 in Elmegreen & Efremov 1997; they referred to the timescale as the “disruption time”), which is consistent with the age of the stars in the regions ($\sim 10^{6.8} \text{ yr}$).

Yamagami & Fujita (2011) also discussed the disruption of the clouds by the Kelvin–Helmholtz (KH) instability via interactions with the ambient ICM. The relation among M_c , P_c , and the cloud radius R_c before star formation starts is given by

$$\frac{M_c}{R_c^2} \sim 190 M_{\odot} \text{ pc}^2 \left(\frac{P_c}{1.38 \times 10^{12} \text{ erg s}^{-1}} \right)^{1/2} \quad (3)$$

(Elmegreen 1989). For the M_c and P_c values that we estimated, the cloud radius was $R_c \sim 43 \text{ pc}$. The timescale of the

development of the KH instability is

$$\tau_{\text{KH}} = \frac{(\rho_c + \rho_{\text{ICM}})R_c}{(\rho_c \rho_{\text{ICM}})^{1/2} v_c}, \quad (4)$$

where $\rho_c = 3M_c/(4\pi R_c^3)$ is the density inside the cloud and v_c is the relative velocity between the cloud and the ICM (Murray et al. 1993). We estimated in Paper I that $\rho_{\text{ICM}} \sim 2.1 \times 10^{-28} \text{ g cm}^{-3}$ and thus we obtain $\tau_{\text{KH}} \sim 1.5 \times 10^7 \text{ yr}$. Since $\tau_{\text{KH}} \sim \tau_{\text{form}}$, the cloud could marginally produce the stars before the KH instability develops. This may indicate that no magnetic fields are required to protect the cloud from the development of the KH instability (Yamagami & Fujita 2011).

4.5. The Nature of HaR-1

From the H α luminosity, the H α ionizing photon emission rate of HaR-1 was $10^{47.41} \text{ s}^{-1}$. Assuming Case B recombination, the logarithm of the total hydrogen ionizing photon emission rate Q_H was $\log(Q_H) \sim 47.8^{+0.15}_{-0.13}$. According to Sternberg et al. (2003), a single B0V dwarf is enough to produce that photon rate; other stars such as B giants and O dwarfs would make too much H α .

However, a single B0V star is insufficient to reproduce the observed NUV magnitude. The absolute V magnitude of a B0V star is -4 (e.g., Wegner 2006). The NUV–V color of B0V was calculated with empirical spectral energy distributions (SEDs) by Pickles (1998) as -1.0 mag . The absolute NUV magnitude is therefore ~ -5 . Meanwhile, the absolute magnitudes of HaR-1 converted from observed NUV magnitudes and the internal extinction correction was $-8.8 \pm 0.7 \text{ mag}$. The observed UV magnitudes were $>3 \text{ mag}$ brighter.

The UV–optical color was also inconsistent with the following models. We calculated the NUV $-i$ color of various SEDs and found that the bluest stars are O9V–B0V (NUV $-i \sim -1.7$). The observed lower limit of the NUV $-i$ color of HaR-1 is NUV $-i < -1.6$ and if we correct for the internal extinction of $E_{\text{gas}}(B - V) = 0.59$, the color is NUV $-i < -2.9$. The model SEDs, the internal extinction estimated from the Balmer decrement, the extinction law, and the factor of 0.44 are therefore inconsistent with the observed color.

5. SUMMARY

In the H I tail of NGC 4388 in the Virgo Cluster, we identified four star-forming systems at a projected distance of 35 kpc and 66 kpc away from the parent galaxy.

Our main results are as follows.

1. The line ratios are reflective of typical H II regions of solar metallicity, with recessional velocities comparable to that of the H I tail, which supports the idea that they are associated with the tail.
2. The H α luminosity and multiband photometry are fit with a burst model (STARBURST99) and we obtained reasonable solutions within 0.3 dex. From the fitting, the mass is $10^{4-4.5} M_{\odot}$ and the age is $\sim 10^{6.8}$ yr, except for the faintest one (HaR-1). The faintest region would have mass smaller than $10^3 M_{\odot}$, and was not well fit, possibly because of stochastic effects.
3. Their young ages and large projected distances mean that the regions were formed after they were removed from their parent galaxy. This supports the theoretical prediction by Yamagami & Fujita (2011). The estimated age and mass and the ram pressure estimated in Paper I suggest that a magnetic field to protect the cloud from KH instability (Yamagami & Fujita 2011) may not be necessary for the clouds.
4. One of the regions, 66 kpc away from NGC 4388 (HaR-2), shows an offset of H α emission from the stars (a fireball feature). This implies that ram pressure is still effective here.
5. Two of the regions (HaR-3,4) are outside of the H I distribution. Evaporation of H I and/or the different deceleration by ram pressure between the H I gas and the condensed region may explain the result.
6. Two of the regions (HaR-1,2) lay at the leading edge of a filamentary dark cloud. The cloud could have been stripped from NGC 4388 by ram pressure. The extinction of the dark cloud is smaller than the internal extinction of the regions. The dust in the dark cloud would be locally dense around the star-forming regions.

As the spectroscopic observations of this study were not a complete sampling of the H α -emitting regions along the tail, we did not investigate the global features in the tail such as the total star formation rate. A future complete survey of the candidates of the star-forming region will quantitatively set constraints on the star formation models in the tail.

We thank Dr. Tom Oosterloo and Dr. Jacqueline van Gorkom for kindly providing us with their map of H I flux and the detailed H I recessional velocity distribution around our targets. We acknowledge the referee, Dr. Giuseppe Gavazzi, for his suggestions and comments. This work is based on observations obtained with the Subaru Telescope. We acknowledge the Subaru staff for their support of the observations. This work has made use of the SDSS-III database, the NED database, the SMOKA archive, the STARS/MASTARS archive,¹⁴ the NOAO science archive, the Mikulski Archive for Space Telescopes (MAST), the NASA/IPAC Infrared Service Archive (IRSA), the MPA-JHU DR7 release of spectrum measurements,¹⁵ the Montage service by IRSA,¹⁶ and the computer systems at the Astronomy Data Center of the NAOJ. Y.F. is supported by KAKENHI (23540308).

¹⁴ <http://stars2.naoj.hawaii.edu/>

¹⁵ <http://www.mpa-garching.mpg.de/SDSS/DR7/>

¹⁶ Funded by the NASA's Earth Science Technology Office, Computational Technologies Project, under Cooperative Agreement Number NCC5-626 between NASA and the California Institute of Technology. The code is maintained by the NASA/IPAC IRSA.

Table 8
Archival Data from Suprime-Cam Used in This Study

| Filter | Date Obs. (UTC) | Exp. Time |
|----------|--------------------|--------------------------------------|
| <i>R</i> | 2002 Jun 05 | 6 minutes \times 6 |
| | 2002 Jun 06 | 6 minutes \times 12 |
| NA659 | 2001 Apr 25 | 5.5 minutes |
| | 2001 Apr 26 | 20 minutes \times 5 |
| <i>V</i> | 2001 Mar 24 | 5 minutes \times 3 |
| NA503 | 2001 Apr 24 | 20 minutes \times 3 |
| <i>i</i> | 2010 Apr 12 | 2.8 minutes \times 5 + 1.4 minutes |

APPENDIX A

DETAILS OF THE PHOTOMETRIC DATA

A.1. Suprime-Cam

The Suprime-Cam data used in the study are summarized in Table 8. The data were retrieved from SMOKA.¹⁷

The data were reduced the same way as in Yoshida et al. (2002). As the *i*-band data were obtained with FDCCDs, crosstalk corrections were applied (Yagi 2012). The World Coordinate System was calibrated using wctools 3.8.3 (Mink 2002) and the Guide Star Catalog 2.3 (Lasker et al. 2008). Photometric zero points were calibrated using the method given in Yagi et al. (2013). We adopted the stars in SDSS-III DR 9 as standard objects and converted the SDSS magnitudes to the Suprime-Cam system. The details of the construction of the magnitude conversion were described in Yagi et al. (2013). The color conversion coefficients from SDSS to Suprime-Cam magnitudes are given in Table 9. Stars of $19 < r < 21$ magnitude in SDSS3 DR9 were used for our calibration. The K-correct (Blanton & Roweis 2007) v4 offset for SDSS¹⁸ is applied; $m_{AB} - m_{SDSS} = 0.012, 0.010$, and 0.028 for *g*, *r*, and *i*, respectively.

In Figures 2 and 3, H α -only images (NB659-*R*) are obtained by subtracting the scaled *R*-band image from the NA659-band image. As the seeing was worse in the *R*-band, the NA659 image was convolved with a Gaussian (FWHM = 0.95 arcsec) to match the size of the point spread function (PSF).

We used SExtractor (Bertin & Arnouts 1996) for the photometry of the Suprime-Cam data. The Galactic extinction was corrected for using the values in NED based on Schlegel et al. (1998) and Schlafly & Finkbeiner (2011): $(A_V, A_R, A_i, A_{NA503}, A_{NA659}) = (0.08, 0.06, 0.05, 0.09, 0.06)$ and $(0.08, 0.06, 0.05, 0.10, 0.07)$ for the HaR-1,2 field and the HaR-3,4 field, respectively. Their magnitudes (MAG_AUTO) after the Galactic extinction correction are given in Tables 2 and 3.

A.2. KPNO 4 m

The NOAO science archive¹⁹ provides calibrated data around the region that were taken on 2007 April 22 and 2007 April 23 with NOAO MOSAIC 1 on the KPNO 4 m Mayall telescope. The data were already used in Kenney et al. (2008). We retrieved the data in rest-H α (ha; center = 6566 Å, FWHM = 80 Å at $F = 3.1$), H α around the Virgo redshift (ha4; center = 6610.1 Å,

¹⁷ <http://smoka.nao.ac.jp/>

¹⁸ <http://howdy.physics.nyu.edu/index.php/Kcorrect>

¹⁹ <http://portal-nvo.noao.edu/>

Table 9
The Coefficients of the Color Conversion

| SDSS-Suprime | CCD | SDSS | range | c_0 | c_1 | c_2 | c_3 | c_4 |
|--------------|------|---------|----------------------|--------|--------|--------|--------|--------|
| $r - NA659$ | MIT | $r - i$ | $0 < r - i < 0.8$ | -0.037 | 0.701 | -0.508 | 0.278 | ... |
| $g - NA503$ | MIT | $g - r$ | $0 < g - r < 0.6$ | -0.046 | -0.228 | -0.101 | ... | ... |
| $g - V$ | SITe | $g - r$ | $-0.4 < g - r < 0.8$ | 0.039 | 0.574 | -0.030 | 0.271 | -0.221 |
| $i - i$ | HPK | $r - i$ | $-0.4 < r - i < 1.6$ | -0.006 | 0.089 | 0.019 | -0.015 | ... |

Table 10
GALEX Tiles and Exposure Times

| Tile | Exp. Time (FUV) | Exp. Time (NUV) | Obs. Date |
|---------------------|--------------------|--------------------|-------------|
| NGA_Virgo_MOS10 | 1590.25 | 3128.45 | 2004 Mar 11 |
| Virgo_Epoque_MOS01 | 482.15 | 15699.9 | 2006 Mar 20 |
| Virgo_Epoque_MOS08 | 504.05 | 16419.85 | 2006 Mar 20 |
| GI5_057013_NGC 4388 | 2538. | 4993.8 | 2009 May 07 |

FWHM = 80 Å at $F = 3.1$), and the R -band (center = 6622 Å, FWHM = 1490 Å at $F = 3.1$). The filter characteristics are given on the KPNO Web site,²⁰ and the center and FWHM were calculated from the transmission data and a 15 Å shift of the R -band at $F = 3.1$.

SExtractor (Bertin & Arnouts 1996) was used for photometry. The photometric zero points were given in the FITS header. We adopted the Galactic extinction of 0.06 for HaR-1 and HaR-2 and 0.07 for HaR-3 and HaR-4. The AB-Vega offset of 0.25 mag was also applied. The results are listed in Table 3.

A.3. *GALEX*

In the *GALEX* archive,²¹ several coadded tiles covered the targets. We retrieved the coadded FITS images listed in Table 10 and measured the flux in a circular aperture in the FUV (1344–1786 Å) and NUV (1771–2831 Å) bands (Morrissey et al. 2007). As the FWHM of the PSF of *GALEX* was large, we adopted an aperture size 6 arcsec in radius. The files presented as *_skybg.fits of each tile was used for the background correction. The background-subtracted aperture fluxes in the tiles were averaged weighted by exposure time and converted to AB magnitudes using the zero point given in Morrissey et al. (2007). We adopted the Galactic extinction correction in the *GALEX* bands given by Wyder et al. (2007): $A_{\text{FUV}} = 8.24E(B - V)$ and $A_{\text{NUV}} = 8.24E(B - V) - 0.67E(B - V)^2$. The results were $A_{\text{FUV}}, A_{\text{NUV}} = (0.206, 0.206), (0.230, 0.231)$ for the HaR-1,2 fields and the HaR-3,4 fields, respectively. The magnitude errors were estimated following the *GALEX* Web site.²² The results are given in Table 2. In the FUV data, HaR-1 shows no recognizable shape. We therefore assumed the measured aperture flux as the upper limit.

A.4. *XMM-OM*

The target fields were also observed by the *XMM-Newton* Optical Monitor (*XMM-OM*) and UVW1 (center = 2905 Å, width = 620 Å; Kuntz et al. 2008) magnitudes of HaR-2,3, and 4 are available in the catalog in the archive. The data were obtained from MAST.²³ The catalog magnitudes are listed

Table 11
XMM-OM

| Name | <i>XMM-OM</i> dataset | UVW1 mag (ABmag) | Date Obs. |
|-------|-----------------------|---------------------|-------------|
| HaR-1 | 0108260201 | ... | 2002 Jul 02 |
| HaR-2 | 0108260201 | 21.9 ± 0.4 | 2002 Jul 02 |
| HaR-3 | 0110930301 | 21.5 ± 0.5 | 2002 Jul 07 |
| HaR-4 | 0110930301 | 21.1 ± 0.3 | 2002 Jul 07 |
| | 0110930701 | 21.2 ± 0.5 | 2002 Dec 12 |

Table 12
AB Magnitudes of HaR-4 from SDSS-DR9

| Object | u | g | r | i | z |
|--------|------------|--------------|--------------|--------------|------------|
| HaR-4 | 22.4 ± 0.5 | 21.31 ± 0.08 | 21.38 ± 0.12 | 21.55 ± 0.16 | 21.6 ± 0.6 |

in Table 11. Although the error on the magnitude was larger than that of *GALEX*, the spatial resolution of *XMM-OM* was higher: the FWHM of the PSF was ~5 arcsec and ~2.3 arcsec for the *GALEX* NUV band and the *XMM-OM* UVW1 band, respectively. We checked that there is no apparent contamination from nearby objects around the targets in the UVW1 band of *XMM-OM*.

A.5. *SDSS*

HaR-4 was detected in SDSS3 DR9 as SDSS J122613.13+124300.4. The SDSS magnitudes are listed in Table 12. We corrected for Galactic extinction and the offset of SDSS magnitudes from AB magnitudes using K-correct, version 4 (Blanton & Roweis 2007); $m_{\text{AB}} - m_{\text{SDSS}} = -0.036, 0.012, 0.010, 0.028$, and 0.040 for the u, g, r, i , and z -bands, respectively. The i -band magnitude was comparable to our measurement in Suprime-Cam in Table 2. The other three HaRs were not detected in SDSS.

We found that the model magnitude of HaR-4 was ~0.7 mag brighter in SDSS DR7 (Abazajian et al. 2009) than that in DR9. The reason could be the difference in the adopted model profile of the object: the Petrosian radius was 7.359 arcsec (DR7) versus 2.475 arcsec (DR9). As seen in the bottom of Figure 3, whose image size is 20 arcsec on a side, the Petrosian radius of 7.3 arcsec was too large for HaR-4 and we considered the magnitude in DR9 to be appropriate.

The ~0.7 mag difference was specific to HaR-4. Other brighter objects had comparable magnitudes. Our photometric calibration of the Suprime-Cam data based on the DR9 data was not affected even if we used the DR7 data.

A.6. *IRAC/Spitzer*

We retrieved calibrated data from the Infrared Array Camera (IRAC) on the *Spitzer Space Telescope* in the 3.6 μm (ch1)

²⁰ <http://www.noao.edu/kpno/mosaic/filters/>

²¹ <http://galex.stsci.edu/GR6/>

²² http://galexgi.gsfc.nasa.gov/docs/galex/FAQ/counts_background.html

²³ <http://archive.stsci.edu/>

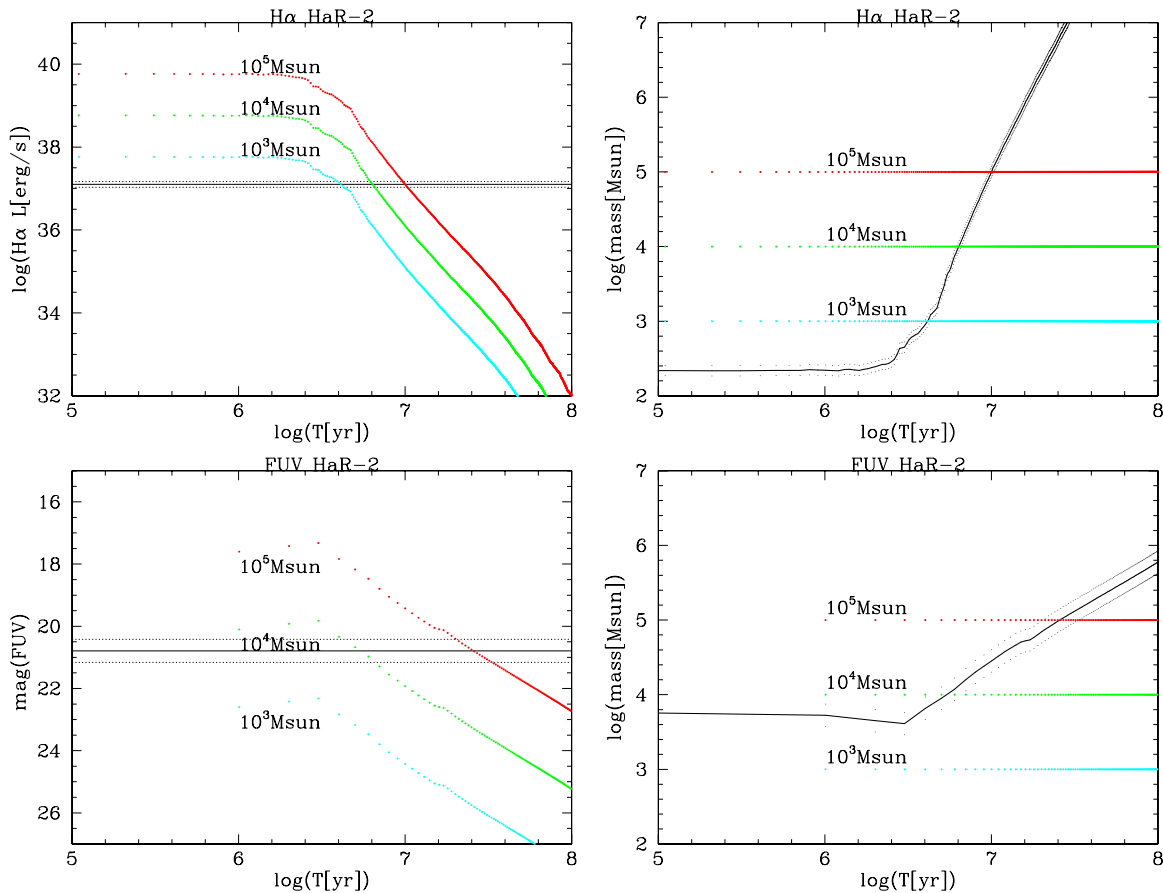


Figure 10. Top left: model $H\alpha$ luminosity of clouds from the STARBURST99 calculation. The Geneva model was adopted. The horizontal lines show the observed luminosity (solid line) and its error (broken line). Top right: transformed from the left figure so that the ordinate is $\log(\text{mass})$. The data were shifted at each age by $-\log(L(H\alpha)/\text{mass})$. Now the observed data are a curve. Bottom left: same as the top left panel, but for FUV magnitude. Bottom right: same as the top right panel, but converted from FUV magnitude by multiplying by -2.5 and shifting by $2.5 \text{ mag}_{\text{FUV}} + \log(\text{mass})$.

(A color version of this figure is available in the online journal.)

and $4.5 \mu\text{m}$ (ch2) channels from IRSA.²⁴ Five images taken in 2010 February and March covered our target fields. Their unique observation identification numbers (AORKEY) and observation dates are listed in Table 13. The exposure times were 93.6 and 96.8 s for ch1 and ch2, respectively.

We used the flux zero point given in the calibrated FITS headers ($1 \text{ DN pixel}^{-1} = 10^6 \text{ Jy sr}^{-1}$). After background subtraction, aperture photometry with a 3 arcsec radius was performed for each target in each image. Then, the median flux was calculated for each target.

The error of each image was estimated from the median of the absolute deviation of random aperture photometry assuming a 3 arcsec radius. AB magnitudes were calculated as

$$\text{AB} = 23.90 - 2.5 \log(S(\mu\text{Jy})). \quad (\text{A1})$$

The results are listed in Table 2.

HaR-1 was not detected in the IRAC images and the aperture flux was negative in some of the images. The upper limit of the aperture flux in a 3 arcsec radius in ch1 ($0.7 \mu\text{Jy}$) was therefore used. HaR-3 was heavily blended with the neighbor galaxy. We tried to measure the flux in a semi-circular aperture to mask the side of the neighbor galaxy and double the flux. The value should still suffer from the envelope of the neighbor galaxy and we regard it as the upper limit of the flux.

APPENDIX B

DETAILS OF THE AGE AND MASS ESTIMATION

For age and mass estimation of HaRs, we used the STARBURST99 v6.0.4 (Leitherer et al. 1999; Vazquez & Leitherer 2005; Leitherer et al. 2010) model and calculated magnitudes and $H\alpha$ luminosities. We adopted a metallicity of $Z = 0.02$, a Kroupa (2001) IMF, an instantaneous burst of a fixed mass, and both Geneva and Padova stellar evolutionary tracks. We also tested a Salpeter IMF (Salpeter 1955), but the result did not change significantly. The spectra were redshifted to the velocity of HaR-2: $z = 0.0074$. We checked that the redshift difference of HaR-1,2 ($z = 0.0074$) and HaR-3,4 ($z = 0.0078$) made only a $<0.001 \text{ mag}$ difference and we neglected the effect.

The model magnitudes were calculated from the spectrum of each age multiplied by the system responses of GALEX, the KPNO mosaic, IRAC, and Suprime-Cam/Subaru. The filter transmittances of GALEX were obtained from COSMOS filter response page,²⁵ where the data were converted from Morrissey et al. (2005). The filter transmittances of IRAC were taken from the *Spitzer* Document page at IRSA.²⁶ The filter transmittances of Suprime-Cam were constructed as the product of the quantum

²⁴ <http://irsa.ipac.caltech.edu/>

²⁵ <http://www.astro.caltech.edu/~capak/cosmos/filters/>

²⁶ <http://irsa.ipac.caltech.edu/data/SPITZER/docs/irac/calibrationfiles/spectralresponse/>

Table 13
Spitzer

| AORKEY | Date Obs. |
|----------|-------------|
| 35323392 | 2010 Mar 11 |
| 35324160 | 2010 Mar 10 |
| 35325184 | 2010 Mar 08 |
| 35325696 | 2010 Mar 03 |
| 35326208 | 2010 Feb 24 |

efficiency of the CCDs,²⁷ the transmittance of the primary focus corrector,²⁸ the reflectivity of the primary mirror,²⁹ the atmospheric extinction model used in Yagi et al. (2013), and the filter responses in Subaru Web site for the *i*-band.³⁰ The simulated filter responses of the KPNO mosaic Ha at the F/3.1 focus were taken from the NOAO Web site.³¹ Note that we did not use V, R, NA503, and NA659 of Suprime-Cam or ha4 of KPNO in this fitting since they would be contaminated by strong nebular emission lines. As the transmittance of Suprime-Cam and the KPNO mosaic was measured in air wavelengths, the model spectra were converted to air wavelengths using the index of Ciddor (1996), when these magnitudes were calculated. The internal extinction was calculated as $E_{\text{star}}(B - V) = 0.44E_{\text{gas}}(B - V)$ (Calzetti et al. 2000), where $E_{\text{gas}}(B - V)$ are given in Table 6. The coefficient $R_{\text{band}} = A_{\text{band}}/E_{\text{star}}(B - V)$ we adopted are (FUV, NUV, V, R, *i*, 3.6 μm , 4.5 μm) = (8.24, 8.24, 3.1, 2.5, 1.9, 0.203, 0.156), respectively.

From the model calculation, we can plot the log of the H α luminosity ($L(\text{H}\alpha)$) as a function of the logarithm of the age T, as in Figure 10 (top left). In the figure, the observed $L(\text{H}\alpha)$ is shown as a solid horizontal line and the 1σ uncertainties of $L(\text{H}\alpha)$ are shown as broken horizontal lines. The crossing is the solution where the model and the observations are consistent. By adding an offset of $-\log(L(\text{H}\alpha)/\text{mass})$ of the model at each age, the figure is transformed so that the ordinate corresponds to the initial mass of the cluster (Figure 10, top right). In the figure, models are horizontal (since the initial mass is time invariant) and the observed value is a curve. The error of the curve comes from the observed value, including the uncertainty of the internal extinction correction; the error is the same at each age. There is no age error at each point.

A similar transformation is applicable to the magnitude plots. For example, the FUV magnitude is plotted in Figure 10 (bottom left). It is converted to the bottom-right panel by multiplying by -2.5 and adding an offset of $-\log(I(\text{FUV})/\text{mass})$ of the model at each age, where $\log(I(\text{FUV})) = -2.5 \text{ mag}_{\text{FUV}}$.

Since the coordinates of the transformed figures (right panels of Figure 10) are the same, we can overplot them in a single figure, with magnitudes in other bands. Figure 8 was thus constructed. The crossing of these curves is the solution where the models and the observations are consistent.

REFERENCES

- Abazajian, K. N., Adelman-McCarthy, J. K., Ageros, M. A., et al. 2009, *ApJS*, **182**, 543
- Abramson, A., Kenney, J. D. P., Crowl, H. H., et al. 2011, *AJ*, **141**, 164
- Ahn, C. P., Alexandroff, R., Allende Prieto, C., et al. 2012, *ApJS*, **203**, 21
- Arnaboldi, M., Freeman, K. C., Okamura, S., et al. 2003, *AJ*, **125**, 514
- Arrigoni Battaia, F., Gavazzi, G., Fumagalli, M., et al. 2012, *A&A*, **543**, A112
- Bertin, E., & Arnouts, S. 1996, *A&AS*, **317**, 393
- Blanton, M. R., & Roweis, S. 2007, *AJ*, **133**, 734
- Boissier, S., Boselli, A., Duc, P.-A., et al. 2012, *A&A*, **545A**, 142
- Boselli, A., & Gavazzi, G. 2006, *PASP*, **118**, 517
- Calzetti, D., Armus, L., Bohlin, R. C., et al. 2000, *ApJ*, **533**, 682
- Calzetti, D., Kinney, A. L., & Storchi-Bergmann, T. 1994, *ApJ*, **429**, 582
- Chung, A., van Gorkom, J. H., Kenney, J. D. P., & Vollmer, B. 2007, *ApJL*, **659**, L115
- Ciddor, P. E. 1996, *ApOpt*, **35**, 1566
- Conselice, C. J., Gallagher, J. S., III, & Wyse, R. F. G. 2001, *ApJ*, **559**, 791
- Cortese, L., Bendo, G. J., Boselli, A., et al. 2010a, *A&A*, **518**, L63
- Cortese, L., Davies, J. I., Pohlen, M., et al. 2010b, *A&A*, **518**, L49
- Cortese, L., Gavazzi, G., Boselli, A., & Iglesias-Paramo, J. 2004, *A&A*, **416**, 119
- Cortese, L., Gavazzi, G., Iglesias-Paramo, J., Boselli, A., & Carrasco, L. 2003, *A&A*, **401**, 471
- Cortese, L., Marcellac, D., Richard, J., et al. 2007, *MNRAS*, **376**, 157
- Crowl, H. H., Kenney, J. D. P., van Gorkom, J. H., & Vollmer, B. 2005, *AJ*, **130**, 65
- Ebeling, H., Edge, A. C., Bohringer, H., et al. 1998, *MNRAS*, **301**, 881
- Elmegreen, B. G. 1989, *ApJ*, **338**, 178
- Elmegreen, B. G., & Efremov, Y. N. 1997, *ApJ*, **480**, 235
- Fossati, M., Gavazzi, G., Boselli, A., & Fumagalli, M. 2012, *A&A*, **544**, A128
- Fujita, Y., & Nagashima, M. 1999, *ApJ*, **516**, 619
- Fujita, Y., Sarazin, C. L., & Sivakoff, G. R. 2006, *PASJ*, **58**, 131
- Fumagalli, M., Gavazzi, G., Scaramella, S., & Franzetti, P. 2011, *A&A*, **528**, A46
- Gavazzi, G., Boselli, A., Mayer, L., et al. 2001, *ApJL*, **563**, L23
- Gavazzi, G., Boselli, A., Vlchez, J. M., Iglesias-Paramo, J., & Bonfanti, C. 2000, *A&A*, **361**, 1
- Gerhard, O., Arnaboldi, M., Freeman, K. C., & Okamura, S. 2002, *ApJL*, **580**, L121
- Giovanelli, R., Haynes, M. P., Kent, B. R., et al. 2007, *AJ*, **133**, 2569
- Grevesse, N., Asplund, M., Sauval, A. J., & Scott, P. 2010, *Ap&SS*, **328**, 179
- Gu, L., Yagi, M., Nakazawa, K., et al. 2013, *ApJL*, **777**, L36 (Paper I)
- Gunn, J. E., & Gott, J. R., III. 1972, *ApJ*, **176**, 1
- Hayashino, T., Tamura, H., Matsuda, Y., et al. 2003, *PNAOJ*, **7**, 33
- Hester, J. A. 2010, *ApJL*, **716**, L14
- Iwasawa, K., Wilson, A. S., Fabian, A. C., & Young, A. J. 2003, *MNRAS*, **345**, 369
- Jansen, R. A., Fabricant, D., Franx, M., & Caldwell, N. 2000, *ApJS*, **126**, 331
- Kapferer, W., Sluka, C., Schindler, S., Ferrari, C., & Ziegler, B. 2008, *A&A*, **499**, 87
- Kapferer, W., Sluka, C., Schindler, S., Ferrari, C., & Ziegler, B. 2009, *A&A*, **499**, 87
- Kashikawa, N., Aoki, K., Asai, R., et al. 2002, *PASJ*, **54**, 819
- Kauffmann, G., Heckman, T. M., Tremonti, C., et al. 2003, *MNRAS*, **346**, 1055
- Kenney, J. D. P., Tal, T., Crowl, H. H., Feldmeier, J., & Jacoby, G. H. 2008, *ApJL*, **687**, L69
- Kewley, L. J., & Dopita, M. A. 2002, *ApJS*, **142**, 35
- Kewley, L. J., Dopita, M. A., Sutherland, R. S., Heisler, C. A., & Trevena, J. 2001, *ApJ*, **556**, 121
- Koda, J., Yagi, M., Boissier, S., et al. 2012, *ApJ*, **749**, 20
- Kong, X., Cheng, F. Z., Weiss, A., & Charlot, S. 2002, *A&A*, **396**, 503
- Kronberger, T., Kapferer, W., Ferrari, C., Unterguggenberger, S., & Schindler, S. 2008, *A&A*, **481**, 337
- Kroupa, P. 2001, *MNRAS*, **322**, 231
- Kuntz, K. D., Harrus, I., McGlynn, T. A., Mushotzky, R. F., & Snowden, S. L. 2008, *PASP*, **120**, 740
- Lasker, B., Lattanzi, M. G., McLean, B. J., et al. 2008, *AJ*, **136**, 735
- Leitherer, C., Ortiz Otálvaro, P. A., Bresolin, F., et al. 2010, *ApJS*, **189**, 309
- Leitherer, C., Schaerer, D., Goldader, J. D., et al. 1999, *ApJS*, **123**, 3
- Lu, N. Y., Hoffman, G. L., Groff, T., Roos, T., & Lamphier, C. 1993, *ApJS*, **88**, 383
- Machacek, M., Jones, C., Forman, W. R., & Nulsen, P. 2006, *ApJ*, **644**, 145
- Machacek, M., Nulsen, P., Stirbat, L., Jones, C., & Forman, W. R. 2005, *ApJ*, **630**, 280
- Mink, D. J. 2002, in ASP Conf. Proc. 281, ADASS XI, ed. D. A. Bohlender, D. Durand, & T. H. Handley (San Francisco, CA: ASP), 169
- Miyazaki, S., Komiyama, Y., Sekiguchi, M., et al. 2002, *PASJ*, **54**, 833
- Morrissey, P., Conrow, T., Barlow, T. A., et al. 2007, *ApJS*, **173**, 682
- Morrissey, P., Schiminovich, D., Barlow, T. A., et al. 2005, *ApJL*, **619**, L7
- Murray, S. D., White, S. D. M., Blondin, J. M., & Lin, D. N. C. 1993, *ApJ*, **407**, 588
- O'Dell, C. R., Ferland, G. J., Henney, W. J., & Peimbert, M. 2013, *AJ*, **145**, 93
- Ohyama, Y., & Hota, A. 2013, *ApJL*, **767**, L29

²⁷ <http://www.naoj.org/Observing/Instruments/SCam/ccd.html>

²⁸ <http://www.naoj.org/Observing/Telescope/Parameters/PFU/>

²⁹ <http://www.naoj.org/Observing/Telescope/Parameters/Reflectivity/>

³⁰ <http://www.naoj.org/Observing/Instruments/SCam/sensitivity.html>

³¹ <http://www.noao.edu/kpno/mosaic/filters/>

- Okamura, S., Yasuda, N., Arnaboldi, M., et al. 2002, *PASJ*, **54**, 883
- Oke, J. B., & Gunn, J. R. 1983, *ApJ*, **266**, 713
- Oosterloo, T., & van Gorkom, J. 2005, *A&A*, **437**, L19
- Osterbrock, D. E., & Ferland, G. J. 2006, *Astrophysics of Gaseous Nebulae and Active Galactic Nuclei* (2nd ed.; Sausalito, CA: University Science Books)
- Owen, F. N., Keel, W. C., Wang, Q. D., Ledlow, M. J., & Morrison, G. E. 2006, *AJ*, **131**, 1974
- Pickles, A. 1998, *PASP*, **110**, 863
- Roediger, E. 2009, *AN*, **330**, 888
- Roediger, E., & Brüggen, M. 2007, *MNRAS*, **380**, 1399
- Roediger, E., & Brüggen, M. 2008, *MNRAS*, **388**, 486
- Roediger, E., Brüggen, M., & Hoeft, M. 2006, *MNRAS*, **371**, 609
- Salpeter, E. E. 1955, *ApJ*, **121**, 161
- Schlaflly, E. F., & Finkbeiner, D. P. 2011, *ApJ*, **737**, 103
- Schlegel, D., Finkbeiner, D. P., & Davis, M. 1998, *ApJ*, **500**, 525
- Sivanandam, S., Rieke, M. J., & Rieke, G. H. 2010, *ApJ*, **711**, 147
- Smith, R. J., Lucey, J. R., Hammer, D., et al. 2010, *MNRAS*, **408**, 1471
- Sternberg, A., Hoffmann, T. L., & Pauldrach, A. W. A. 2003, *ApJ*, **599**, 1333
- Sun, M., Donahue, M., Roediger, E., et al. 2010, *ApJ*, **708**, 946
- Sun, M., Donahue, M., & Voit, G. M. 2007, *ApJ*, **671**, 190
- Sun, M., Jones, C., Forman, W., et al. 2006, *ApJL*, **637**, L81
- Sun, M., & Vikhlinin, A. 2005, *ApJ*, **621**, 718
- Tonnesen, S., & Bryan, G. L. 2012, *MNRAS*, **422**, 1609
- van Dokkum, P. G. 2001, *PASP*, **113**, 1420
- Vazquez, V. A., & Leitherer, C. 2005, *ApJ*, **621**, 695
- Vollmer, B. 2009, *A&A*, **502**, 427
- Vollmer, B., Braine, J., Pappalardo, C., & Hily-Blant, P. 2008, *A&A*, **491**, 455
- Vollmer, B., & Huchtmeier, W. 2007, *A&A*, **462**, 93
- Vollmer, B., Soida, M., Braine, J., et al. 2012, *A&A*, **537**, A143
- Wang, Q. D., Owen, F., & Ledlow, M. 2004, *ApJ*, **611**, 821
- Wegner, W. 2006, *MNRAS*, **371**, 185
- Weżgowiec, M., Vollmer, B., Ehle, M., et al. 2011, *A&A*, **531**, A44
- Wyder, T. K., Martin, D. C., Schiminovich, D., et al. 2007, *ApJS*, **173**, 293
- Yagi, M. 2012, *PASP*, **124**, 1347
- Yagi, M., Komiyama, Y., Yoshida, M., et al. 2007, *ApJ*, **660**, 1209
- Yagi, M., Suzuki, N., Yamanoi, H., et al. 2013, *PASJ*, **65**, 22
- Yagi, M., Yoshida, M., Komiyama, Y., et al. 2010, *AJ*, **140**, 1814
- Yamagami, T., & Fujita, Y. 2011, *PASJ*, **63**, 1165
- Yoshida, M., Ohyama, Y., Iye, M., et al. 2004, *AJ*, **127**, 90
- Yoshida, M., Yagi, M., Komiyama, Y., et al. 2008, *ApJ*, **688**, 918
- Yoshida, M., Yagi, M., Komiyama, Y., et al. 2012, *ApJ*, **479**, 43
- Yoshida, M., Yagi, M., Okamura, S., et al. 2002, *ApJ*, **567**, 118